Cell

Resource

Trellis tree-based analysis reveals stromal regulation of patient-derived organoid drug responses

Graphical abstract

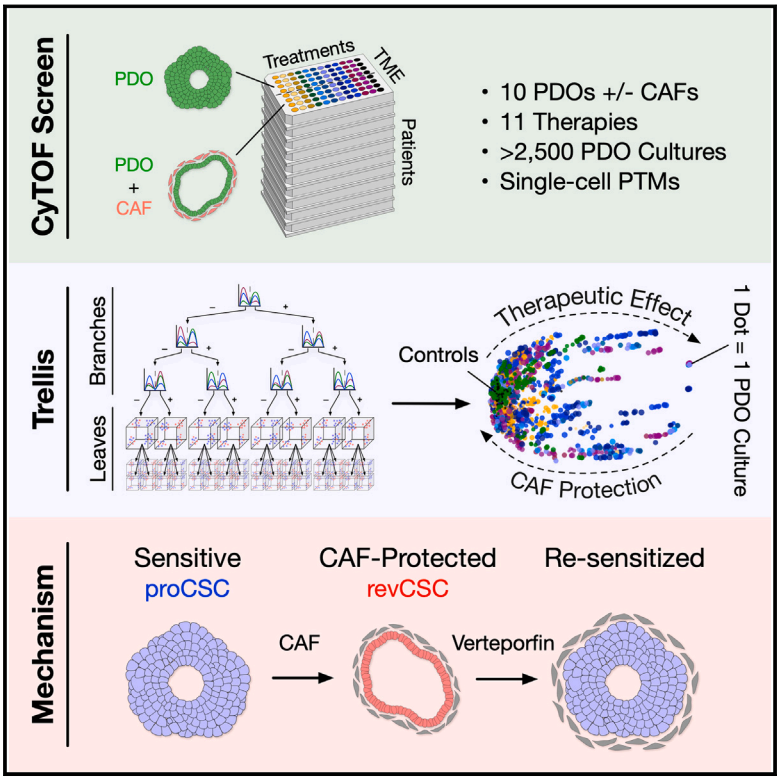

Authors

María Ramos Zapatero, Alexander Tong, James W. Opzoomer, ..., Daniel Hochhauser, Smita Krishnaswamy, Christopher J. Tape

Correspondence

smita.krishnaswamy@yale.edu (S.K.), c.tape@ucl.ac.uk (C.J.T.)

In brief

Single-cell signaling analysis of >2,500 patient-derived organoid (PDO) and cancer-associated fibroblast (CAF) cultures using a method called Trellis reveals patient-specific drug responses. CAFs can protect PDOs by polarizing proliferative colonic stem cells to slow-cycling revival stem cells.

Highlights

- >2,500 single-cell signaling responses from drug-treated PDOs and CAFs
- Trellis: tree-based treatment effect method for single-cell screening analysis
- PDOs have patient- and CAF-specific drug responses that align with PTM signaling
- CAFs can polarize PDOs to a chemorefractory revival stem cell (revCSC) fate

Ramos Zapatero et al., 2023, Cell *186*, 5606–5619
December 7, 2023
https://doi.org/10.1016/j.cell.2023.11.005

CellPress

CellPress
OPEN ACCESS

Cell

Resource

Trellis tree-based analysis reveals stromal regulation of patient-derived organoid drug responses

María Ramos Zapatero,[1,11] Alexander Tong,[2,3,4,11] James W. Opzoomer,[1] Rhianna O'Sullivan,[1] Ferran Cardoso Rodriguez,[1] Jahangir Sufi,[1] Petra Vlckova,[1] Callum Nattress,[1] Xiao Qin,[1] Jeroen Claus,[5] Daniel Hochhauser,[6] Smita Krishnaswamy,[2,7,8,9,10,12,*] and Christopher J. Tape[1,12,13,*]

[1]Cell Communication Lab, Department of Oncology, University College London Cancer Institute, London WC1E 6DD, UK
[2]Department of Computer Science, Yale University, New Haven, CT, USA
[3]Department of Computer Science and Operations Research, Université de Montréal, Montreal, QC, Canada
[4]Mila – Quebec AI Institute, Montréal, QC, Canada
[5]Phospho Biomedical Animation, The Greenhouse Studio 6, London N17 9QU, UK
[6]Drug-DNA Interactions Group, Department of Oncology, University College London Cancer Institute, London WC1E 6DD, UK
[7]Department of Genetics, Yale University, New Haven, CT, USA
[8]Program for Computational Biology & Bioinformatics, Yale University, New Haven, CT, USA
[9]Program for Applied Math, Yale University, New Haven, CT, USA
[10]Wu-Tsai Institute, Yale University, New Haven, CT, USA
[11]These authors contributed equally
[12]Senior author
[13]Lead contact
*Correspondence: smita.krishnaswamy@yale.edu (S.K.), c.tape@ucl.ac.uk (C.J.T.)
https://doi.org/10.1016/j.cell.2023.11.005

SUMMARY

Patient-derived organoids (PDOs) can model personalized therapy responses; however, current screening technologies cannot reveal drug response mechanisms or how tumor microenvironment cells alter therapeutic performance. To address this, we developed a highly multiplexed mass cytometry platform to measure post-translational modification (PTM) signaling, DNA damage, cell-cycle activity, and apoptosis in >2,500 colorectal cancer (CRC) PDOs and cancer-associated fibroblasts (CAFs) in response to clinical therapies at single-cell resolution. To compare patient- and microenvironment-specific drug responses in thousands of single-cell datasets, we developed "Trellis"—a highly scalable, tree-based treatment effect analysis method. Trellis single-cell screening revealed that on-target cell-cycle blockage and DNA-damage drug effects are common, even in chemorefractory PDOs. However, drug-induced apoptosis is rarer, patient-specific, and aligns with cancer cell PTM signaling. We find that CAFs can regulate PDO plasticity—shifting proliferative colonic stem cells (proCSCs) to slow-cycling revival colonic stem cells (revCSCs) to protect cancer cells from chemotherapy.

INTRODUCTION

Tumors are heterogeneous cellular systems comprising cancer cells, stromal fibroblasts, and various immune cells. Tumor phenotypes are regulated by cell-intrinsic mutations within cancer cells and cell-extrinsic cues from the tumor microenvironment (TME).[1] Colorectal cancer (CRC) kills >0.9 million people per year worldwide[2] and is characterized by high inter-patient genetic heterogeneity and patient-specific responses to therapy.[3] Cancer-associated fibroblasts (CAFs) are one of the most profuse cell types in the CRC TME,[4] and high CAF abundance correlates with poor overall survival[5] and influences response to both targeted therapies[6] and radiotherapy.[7] Unfortunately, how CAFs regulate cancer cell therapy responses in a patient-specific manner is poorly understood.

Patient-derived organoids (PDOs) are personalized cancer models[8] that can mimic their parent tumors' response to chemotherapies,[9] with several studies proposing PDOs as personalized avatars of drug response.[10] However, epithelial PDO monocultures cannot model the influence of stromal cells on therapy response. PDOs can be co-cultured with stromal and immune cells to recapitulate elements of the TME,[11] but how this alters PDO phenotypes and drug response mechanisms is unknown. Moreover, PDO drug sensitivity is typically measured using bulk live/dead viability assays[12] that cannot resolve cell-type-specific data from co-cultures and provide no mechanistic insight into drug responses.[13]

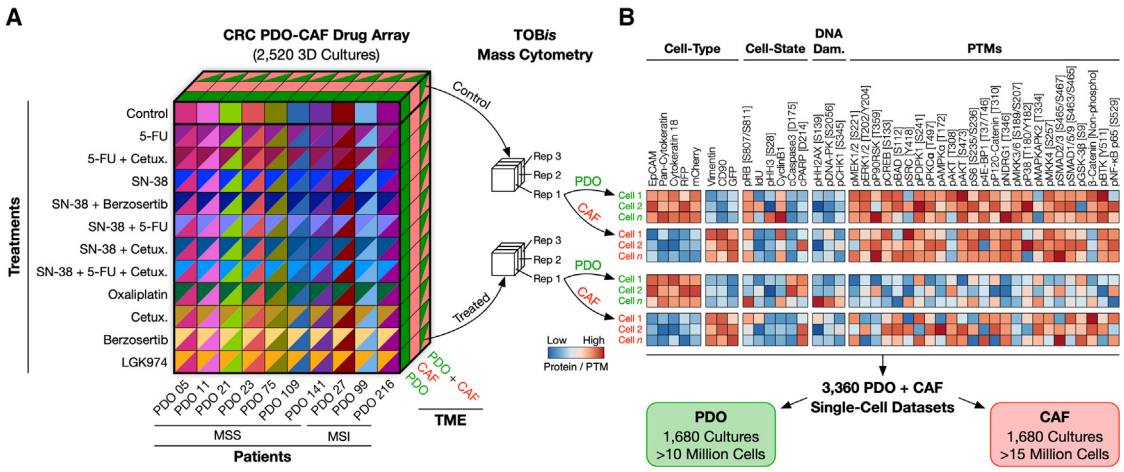

Figure 1. TOB*is* mass cytometry single-cell PTM PDO-CAF drug screening

(A) Multidimensional array of 10 CRC PDOs (7 microsatellite stable [MSS], 3 microsatellite unstable [MSI]) treated with 11 titrated drug combinations either alone or in co-culture with CRC CAFs in three replicates (Rep) (2,520 3D cultures).

(B) PDO-CAFs were barcoded *in situ* using TOB*is*; stained with 44 rare-earth metal antibodies spanning cell-type identification, cell state, DNA-damage response, and PTM signaling; and analyzed by mass cytometry (3,360 single-cell PTM datasets).

See also Tables S1, S2, and S3.

To overcome these limitations, here we developed a highly multiplexed Thiol-reactive Organoid Barcoding *in situ* (TOB*is*) mass cytometry[14,15] platform to study how anti-cancer therapies regulate the post-translational modification (PTM) signaling, DNA-damage, cell-cycle, and apoptosis response of CRC PDOs in the presence or absence of CAFs at single-cell resolution across >2,500 PDO-CAF cultures. To compare single-cell drug responses from thousands of cell-type-specific datasets, we developed "Trellis," a tree-based treatment effect analysis method that derives generalized optimal transport distances between samples after normalizing by their own controls. TOB*is* mass cytometry and Trellis single-cell screening revealed that drug-induced PTM signaling responses are PDO-specific and demonstrated that CAFs shift epithelial cells toward a slow-cycling revival stem cell fate to protect CRC cells from chemotherapy. CAF chemoprotection could be rationally reversed using insights from single-cell PTM data, demonstrating the utility of mechanism-focused drug screening for overcoming therapy resistance. These results illustrate the functional intertumoral heterogeneity of patient-specific drug response mechanisms and highlight the role of TME cells in regulating drug resistance plasticity in cancer.

RESULTS

Patient- and microenvironment-specific single-cell PTM PDO-CAF drug screening

To study how CAFs regulate patient-specific drug response signaling, we established a high-throughput 3D organoid co-culture system comprising 10 CRC PDOs[12] (Table S1) cultured either alone or with CRC CAFs.[16,17] Organoid cultures were treated in triplicate with either vehicle control or titrated combinations of clinical therapies 5-fluorouracil (5-FU), SN-38 (active metabolite of Irinotecan), Oxaliplatin, and Cetuximab (EGFR inhibitor). LGK974 (PORCN inhibitor)[12] was also studied to investigate PDO-CAF WNT signaling and Berzosertib (VX-970), as ATR inhibition has been hypothesized to synergize with DNA-damaging agents in CRC[18] (Figure 1A; Table S2). Following treatment, each culture was fixed *in situ*, stained with thiol-reactive monoisotopic TOB*is* barcodes,[15] pooled, dissociated into single cells, stained with a panel of 44 rare-earth metal antibodies (identifying cell type, cell state, DNA damage, and PTM signaling; Table S3), and analyzed by mass cytometry (Figure 1B). Following multiplexed debarcoding[19] and cell-type-specific gating, we obtained >10 million PDO cells and >15 million CAFs from 2,520 3D cultures (3,360 cell-type-specific single-cell PTM signaling datasets).

Trellis: Tree-based single-cell treatment effect analysis

To understand how PDO-CAF communication affects therapeutic response, we face the challenge of comparing 3,360 single-cell datasets. To address this, we use optimal transport, a rigorous mathematical framework for comparing large high-dimensional datasets.[20] The idea of optimal transport is to treat high-dimensional datasets as piles of dirt and compute the cost of transporting one pile to the other in the most efficient way possible. This cost is then considered the "earth mover's distance" (EMD) between two data samples. However, there are several analytical challenges when applying optimal transport to large single-cell screening data. First, existing EMD methods use the manifold structure of transcriptomic technologies, embodied as an affinity of nearest neighbor graphs to define EMD based on manifold distances.[21–23] However, in cytometry data, antibody panels are designed to delineate specific cell types and cell states and analyzed using gating strategies that follow a tree structure. This leads to a data topology better described by tree distances rather than a smooth manifold or a graph discretization of such a manifold. Second, our single-cell

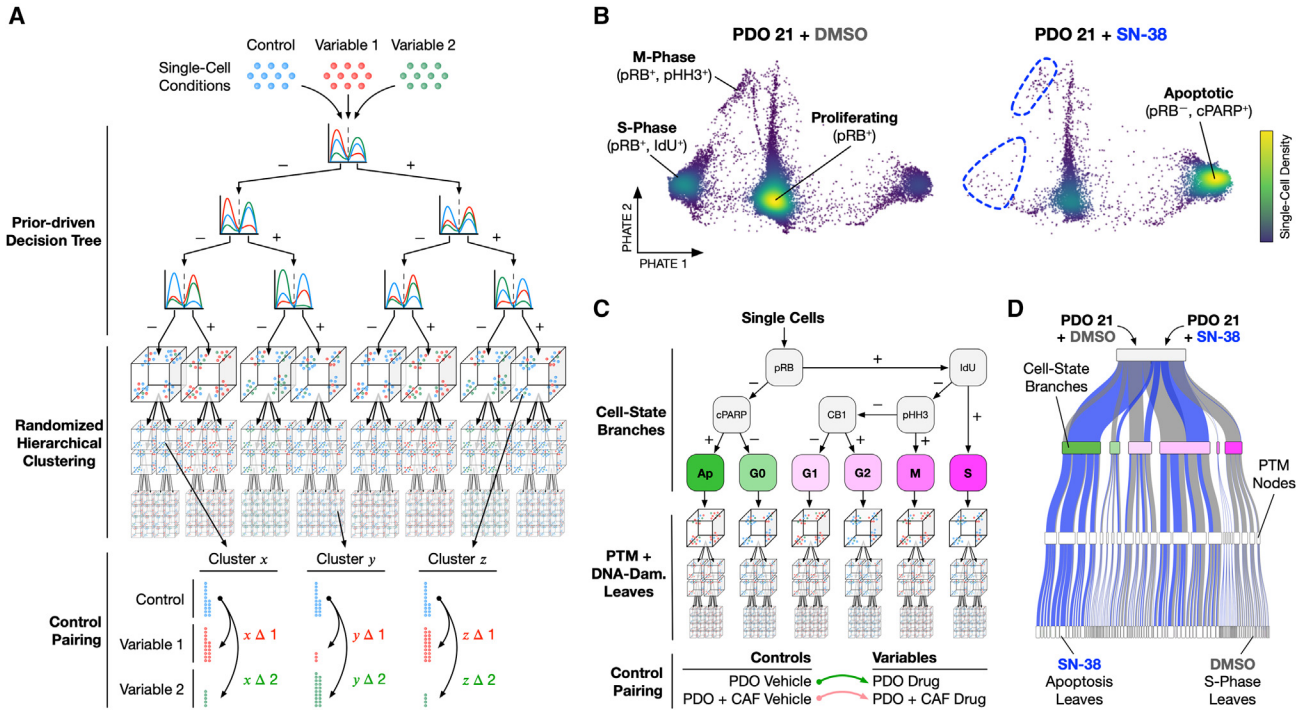

Figure 2. Trellis: Tree-based single-cell treatment effect analysis

(A) Single cells from control and variable conditions are distributed through a decision tree based on markers selected based on prior biological knowledge and experimental design. This decision tree supervenes upon randomized *k*-means clustering nodes. The first decision tree weighs cytometry gating strategies, while randomized hierarchical clustering leverages latent parameters. In each node of the tree, variables are subtracted from paired controls to create a multi-scaled differential matrix that scales to thousands of conditions.

(B) Single-cell density PHATE embeddings of PDO 21 treated with DMSO or SN-38 (irinotecan). SN-38 results in cell-cycle exit (IdU^-, $pHH3^-$, and pRB^-) and induction of apoptosis ($cPARP^+$).

(C) Trellis analysis for single-cell PDO on-target drug responses leveraging cell-state branches and randomized PTM and DNA-damage parameters. Paired Trellis scores are calculated per PDO by comparing untreated controls to drugs for both mono-cultures and co-cultures. CB1, Cyclin B1.

(D) Sankey diagram showing data from (B) distributing through the Trellis layout in (C) (terminal layer of clusters not shown).

See also Figures S1–S3.

PDO-CAF screen compares independent systems (e.g., patients, microenvironments, and/or technical batches) perturbed by common drug treatments. To derive a common treatment effect across all 3,360 conditions, we therefore need to compare each drug treatment to its own internal control in a common space.

To solve these problems, we developed Trellis, a method that embeds cytometry data into a partially randomized decision tree that accounts for control samples and defines a generalized EMD distance on a random forest of such trees (Figure 2A). First, Trellis leverages the design of cytometry experiments by using a fixed gating tree that captures hierarchies inherent in the marker panel. Designing a decision tree using selected markers (e.g., cell type or cell state) enables an automated assessment of cell populations that mimics human intuition in the design of the experiment and subsequently its interpretation. Trellis can leverage gating strategies that use single or multiple trees (Algorithm 1, line 3). Following the supervised decision tree, data points are hierarchically clustered based on the intensities of the remaining markers. Trellis then creates embeddings of all conditions by projecting data points onto these decision trees and thus populating the nodes and leaves of the trees with data densities (Algorithm 1, lines 4 and 5). Second, "paired" Trellis allows variables to be compared to controls by subtracting their relative densities at all intermediate nodes and leaves (Algorithm 1, line 6; Figure 2A). Finally, Trellis allows an EMD to be defined on these measures, which are not necessarily positive (due to control subtraction), by simply measuring a

Algorithm 1. Trellis algorithm for comparing single-cell treatment effects

1: **Input:** Dataset containing single-cell expression values for all controls and variables.
2: **Output:** Distances between treatment effects to their relative controls.
3: Build decision tree incorporating experimental design on known markers followed by random construction with edge weights w for each node.
4: Embed each condition to a vector with each element as proportion of cells in intermediate node or leaf forming abundance matrix $\boldsymbol{A}$.
5: Multiply element-wise $w \otimes \boldsymbol{A}$ to calculate Trellis embeddings $\boldsymbol{E}$.
6: (optionally) Subtract relevant control vectors for paired Trellis embeddings $\tilde{\boldsymbol{E}}$.
7: **return** Relevant L^1 distances between embeddings.

weighted distance between the node populations. Therefore, paired Trellis enables thousands of single-cell samples to be compared to their internal controls in a common space—enabling clear distinction of individual treatment effects in paralleled high-dimensional single-cell screening data (Figure S1).

Trellis pairing treatments to controls enables paralleled visualization of treatment effects (Figure S1A) and reduces batch effects in serially acquired single-cell screening data (Figure S1B). Experimentally designed branches further resolve biologically important treatment effects compared to fully randomized trees (Figures S1C and S1D). Trellis outperforms existing single-cell treatment effect methods (Figure S2A), and the tree domain structure enables thousands of single-cell datasets to be analyzed rapidly (Figure S2B) and accurately (Figure S2C). Experimentally designed branches are customizable to different biological questions, and Trellis recapitulates features of published datasets (Figure S2D). Trellis is therefore a fast, scalable, and accurate treatment effect analysis method for analyzing large-scale single-cell cytometry screening data. Further details on Trellis' scalability, theoretical soundness, and robustness can be found in STAR Methods.

Trellis single-cell analysis of PDO cell state and PTM signaling

Anti-cancer drugs typically induce major shifts in cell cycle and apoptosis that can be detected by mass cytometry. For example, SN-38 inhibits topoisomerase 1,[24] resulting in S-phase blockage (IdU^-), cell-cycle exit (pRB^-), and induction of apoptosis ($cPARP^+$) (Figure 2B). Similarly, 5-FU blocks nucleotide biosynthesis by inhibiting thymidylate synthase,[25] which subsequently stalls S-phase entry, whereas oxaliplatin induces ribosome biogenesis stress to block mitotic progression[26] (Figures S3A–S3D). Capturing shifts in cell state is therefore crucial for understanding on-target drug responses in single-cell data.

In mass cytometry, cell state is identified by hierarchical gating of pRB, IdU, pHH3, Cyclin B1, and cPARP/cCaspase-3[27,28] and is therefore well suited for Trellis branches. For cell-type-specific analysis of PDO-CAF co-cultures, we designed a Trellis tree using a cell-state-driven decision tree that supervenes upon randomized DNA damage and PTM signaling hierarchical clustering (Figures 2C and S3E). When cell-state markers are used for the decision tree, the subsequent unsupervised clustering tree is only performed with PTM and DNA-damage markers. This tree topology sensitizes Trellis to canonical on-target drug-induced shifts in cell cycle and apoptosis while also leveraging latent changes in DNA damage and PTM signaling (Figures 2D and S3A–S3D).

Trellis analysis of cell-type-specific PDO-CAF drug responses

We used paired Trellis to analyze 3,360 (1,680 PDO, 1,680 CAF) single-cell PTM profiles (>25 million single cells; Figure 3A), exploring drug-, patient-, and microenvironment-specific therapy responses for both PDOs (Figures 3B–3D) and CAFs (Figures S3F–S3I). Since paired Trellis performs pairwise normalization to internal controls, all controls group on the left side of the PHATE (potential of heat diffusion for affinity-based transition embedding) graph (Figures 3B and S1A), and treatments embed relative to their controls, depending on their distribution through the Trellis tree. This enables therapeutic effects to be visualized across PHATE 1 and mechanistic response in PHATE 2 (Figure S4A).

If the same drug were to have an equal effect on all PDOs, Trellis would group each condition by drug type. However, we found that PDO treatment effects are characterized not by drug type, but by patient-specific signaling responses (Figures 3C and S4B). We observed four patient-grouped responses to 5-FU, SN-38, and oxaliplatin chemotherapies: (1) broadly chemosensitive with high apoptosis (PDOs 21 and 75), (2) broadly chemosensitive with apoptosis and a strong DNA damage response (PDOs 23 and 27), (3) anecdotally chemosensitive (i.e., only apoptotic with a specific drug; PDOs 99 and 109), and (4) chemorefractory with minimal apoptosis and low DNA damage response (PDOs 05, 11, 141, and 216; Figures 3C and S4B). Cetuximab, Berzosertib, and LGK974 generally had modest effects on PDO cell state and PTMs relative to chemotherapies (Figure 3B). While PDOs demonstrate clear patient- and microenvironment-specific drug responses, CAF signaling did not cluster by patient or drug (Figures S3F–S3I), suggesting chemotherapies mainly alter the cell state, DNA damage, and PTM profiles of PDOs, not CAFs. Intriguingly, Trellis also revealed CAFs protect some PDOs from chemotherapies (Figure 3D).

PDO drug signaling responses are patient-specific

PDOs have been proposed as personalized avatars of drug response,[10] but how clinical treatments mechanistically alter patient-specific PDO biology is not well understood. To explore patient-specific drug response signaling, we updated the Trellis decision tree by combining cell-state parameters with a pHH2AX [S139] detection layer to enrich on-target DNA double-strand breaks and analyzed each patient drug response in parallel (Figures S5A–S5D). Patients continue to display either broad (PDOs 21, 23, 27, and 75) or anecdotal (PDOs 99 and 109) chemotherapeutic sensitivity and multiple examples of drug insensitivity (Figure 4A).

Unlike univariate live/dead metrics used in traditional drug screens, TOB*is* mass cytometry can detect on-target treatment effects that do not result in cell death. For example, we observed that SN-38 induces on-target M- and S-phase blockage and double-strand breaks in both PDO 21 and PDO 05, yet only PDO 21 translates genotoxic stress into apoptosis (Figure 4B). Similarly, in PDOs 23 and 99, 5-FU and SN-38 result in a large DNA damage response and stalled mitosis, respectively, but not apoptosis (Figure S5E). 5-FU and SN-38 can clearly induce double-strand breaks and cell-cycle arrest in these PDOs, but they do not translate genotoxic replication stress into cell death. In fact, chemotherapies display on-target mitotic arrest in nearly all PDOs (83%), but only a subset of patient and treatment combinations trigger apoptosis (40%; Figures S5F–S5H). This suggests on-target drug responses are common in CRC PDOs but are often insufficient to induce cell death.

The patient-specific drug sensitivity demonstrated by several PDOs reinforces the notion that PDOs could be used to identify drugs uniquely potent to an individual's cancer. For example, in

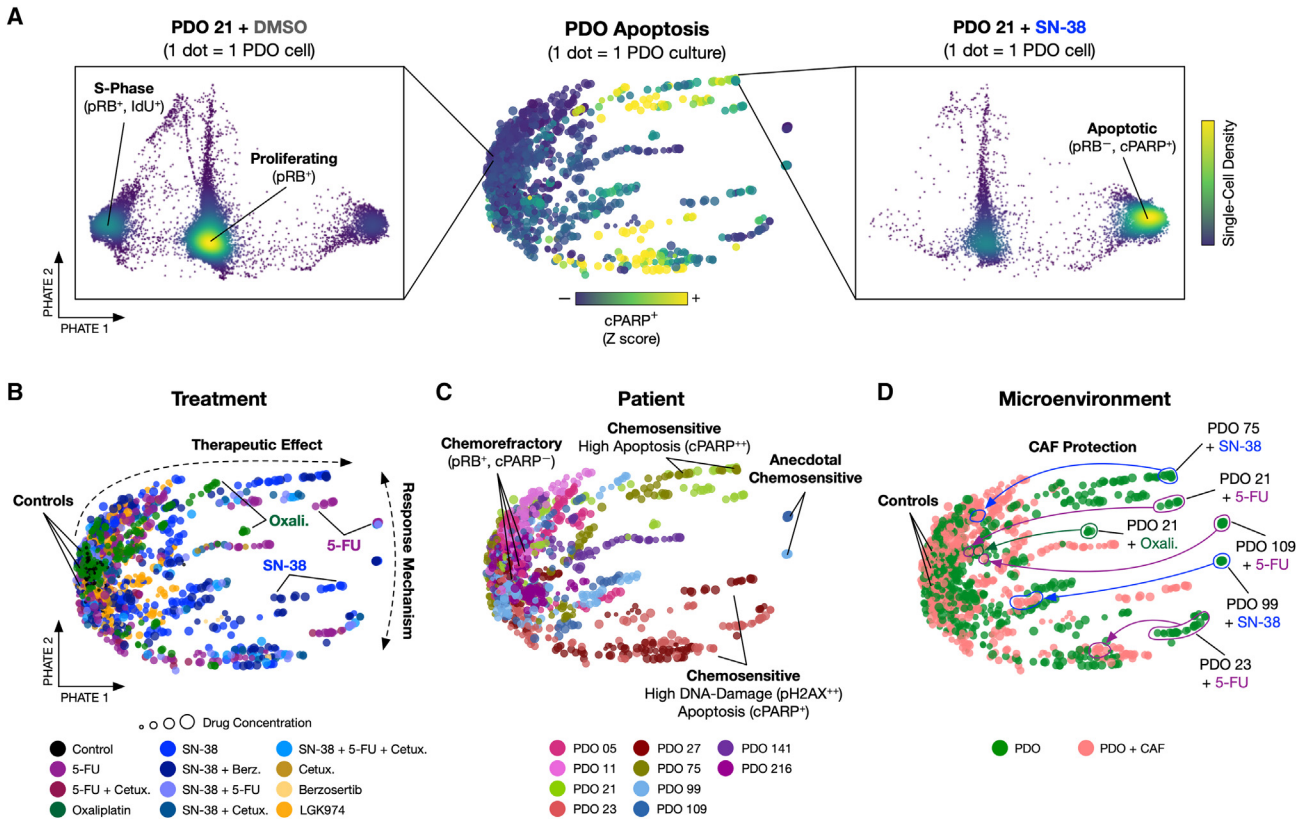

Figure 3. Trellis analysis of single-cell PDO-CAF drug responses

(A) Trellis-PHATE of 1,680 PDO single-cell PTM profiles (1 dot = 1 organoid culture comprising >5,000 single cells) colored by apoptosis with representative single-cell density embeddings of PDO 21 + DMSO or + SN-38. Single-cell plots are calculated with PHATE on 34 dimensions (raw intensities of cell state, PTMs, and DNA-damage markers), while Trellis plots (1 dot = 1 condition) are calculated by PHATE based on 504 dimensions (paired abundance matrix of cells from each condition along each node of the tree).

(B) PDO drug-treatment-specific responses. Controls used for pairing group on the left, with treatment effects spreading across PHATE 1 and response mechanisms resolving across PHATE 2.

(C) Patient-specific drug responses illustrate different chemosensitive mechanisms and chemorefractory patients.

(D) CAFs provide patient-specific chemoprotection from 5-FU, SN-38, and oxaliplatin.

See also Figures S3 and S4.

PDO 99, 5-FU blocks mitosis and SN-38 causes a large DNA damage response—yet neither chemotherapy induces substantial apoptosis. However, when treated with oxaliplatin, PDO 99 exits the cell cycle and enters apoptosis (Figure S5E). Unlike 5-FU and SN-38, oxaliplatin does not kill cells directly through blocking S-phase, but rather via inducing ribosome biogenesis stress.[26] PDO 99 appears refractory to cytostatic stress but hypersensitive to ribosome biogenesis stress. Similarly, ATR inhibitors block single-stranded DNA damage response and typically synergize with DNA-damage-inducing drugs.[18] However, we find Berzosertib only increases SN-38-induced apoptosis in microsatellite unstable (MSI) PDOs (Figure S5I), suggesting ATR inhibitors might only be effective in MSI CRC patients.

Chemosensitive PDOs have distinct cell-intrinsic PTM signaling

We next sought to understand features common to chemosensitive and chemorefractory PDOs. Therapeutic response does not correlate with MSI/MSS (microsatellite stable) status, clinical staging, anatomical location, or *KRAS*/*APC* genotypes (Figures S4C and S4D; Table S1). However, we found that baseline PDO cell state and PTM signaling are patient-specific and align with chemosensitivity (Figures 4C, S4C, and S4D). Chemosensitive PDOs 21, 23, 27, and 75 are highly proliferative at baseline and experience canonical S-phase blockage, increased DNA damage, and apoptosis when treated with both 5-FU and SN-38. In contrast, chemorefractory PDOs are slow-cycling (Figure 4C). When treated with 5-FU, SN-38, and oxaliplatin, chemorefractory PDOs undergo a reduction in S-phase and blocked M-phase consistent with on-target drug responses but generally elicit a lower double-strand break response compared to chemosensitive patients and do not activate PARP or Caspase-3 (Figures 4D and 5E). This suggests that even chemorefractory PDOs experience on-target drug responses, but their slow mitotic signaling flux means drug-induced cytostatic stress cannot trigger widespread DNA damage and apoptosis. We found that chemorefractory PDOs typically have high levels of

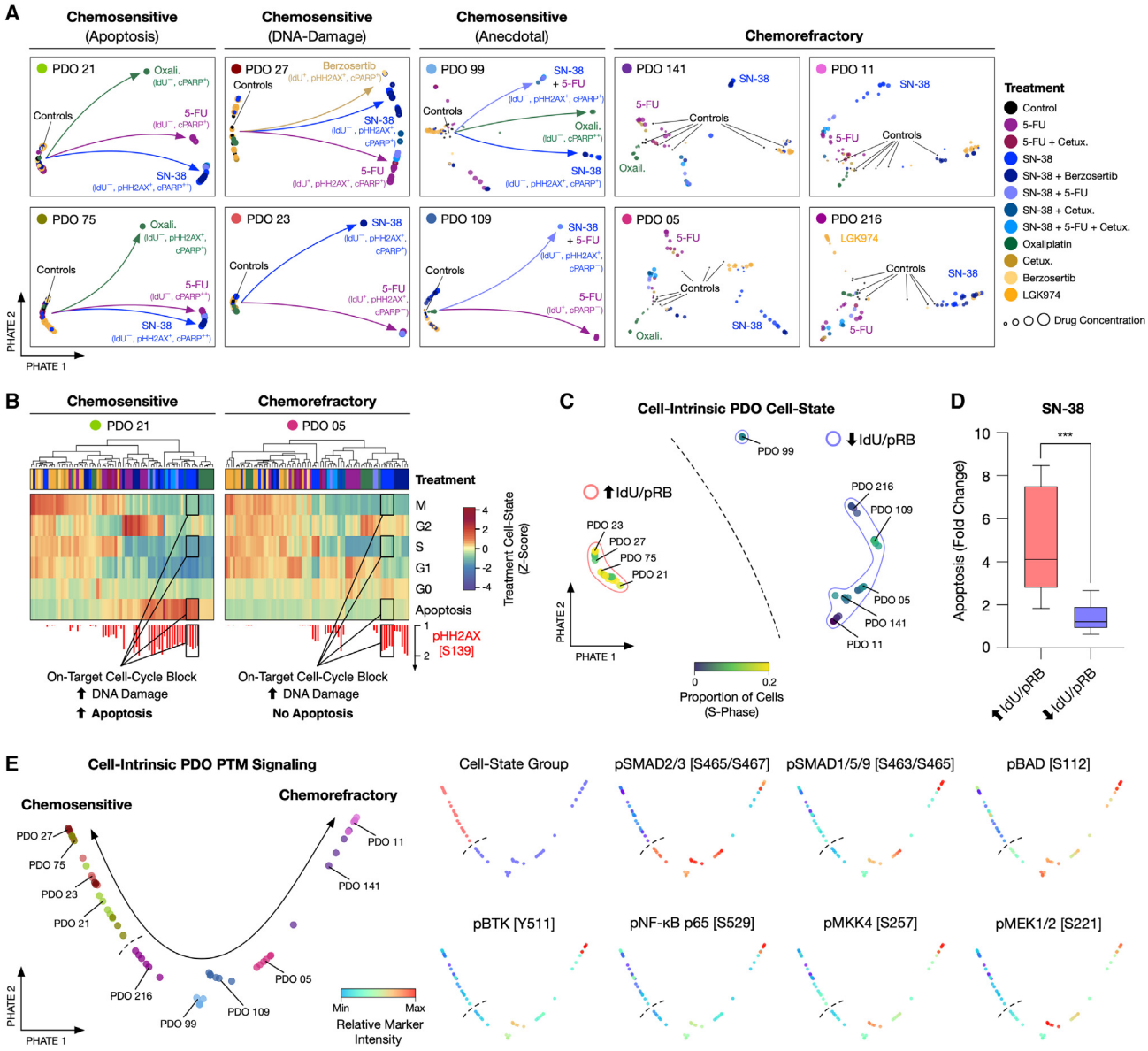

Figure 4. PDO drug response mechanisms are patient-specific and align with cell-intrinsic cell state and PTM signaling

(A) Trellis-PHATE patient-specific PDO drug responses (840 single-cell PTM datasets).

(B) Patient-specific distribution of cells within Trellis branches reveals on-target cell-state shifts upon drug treatments. Treatment cell state quantifies the fold change of the proportion of cells/cell state over the controls for each treatment (*Z* score). DNA damage is quantified by the fold change of the proportion of $pHH2AX^+$ cells over controls.

(C) Trellis-PHATE resolves high IdU/pRB (red outline) and low IdU/pRB (blue outline) cell-intrinsic cell state PDO groups (colored by proportion of cells in S-phase).

(D) SN-38-induced apoptosis in low IdU/pRB and high IdU/pRB PDOs. Unpaired *t* test, *** < 0.001.

(E) TreEMD-PHATE of cell-intrinsic PTM signaling nodes demonstrates PTMs up-regulated in chemorefractory PDOs.

See also Figure S5.

cell-intrinsic pSMAD2/3, pSMAD1/5/9, pMKK4, pBAD, pBTK, and pNF-κB signaling (Figure 4E)—suggesting these pathways relate to a chemorefactory cell state. In summary, TOB*is* mass cytometry and Trellis reveal that on-target drug activity is common in CRC PDOs (even in chemorefractory PDOs), but cytotoxicity is patient-specific and correlates with cell-intrinsic PDO cell states and PTM signaling.

CAF-chemoprotected PDOs have altered PDO PTM signaling

CAFs have both pro- and anti-cancer roles across a variety of solid tumors, but to what extent these effects are patient-specific is poorly understood.[4] To functionally explore the role of CAFs in patient-specific CRC PDO drug responses, we performed paralleled Trellis analysis of PDO monocultures and PDO-CAF co-cultures

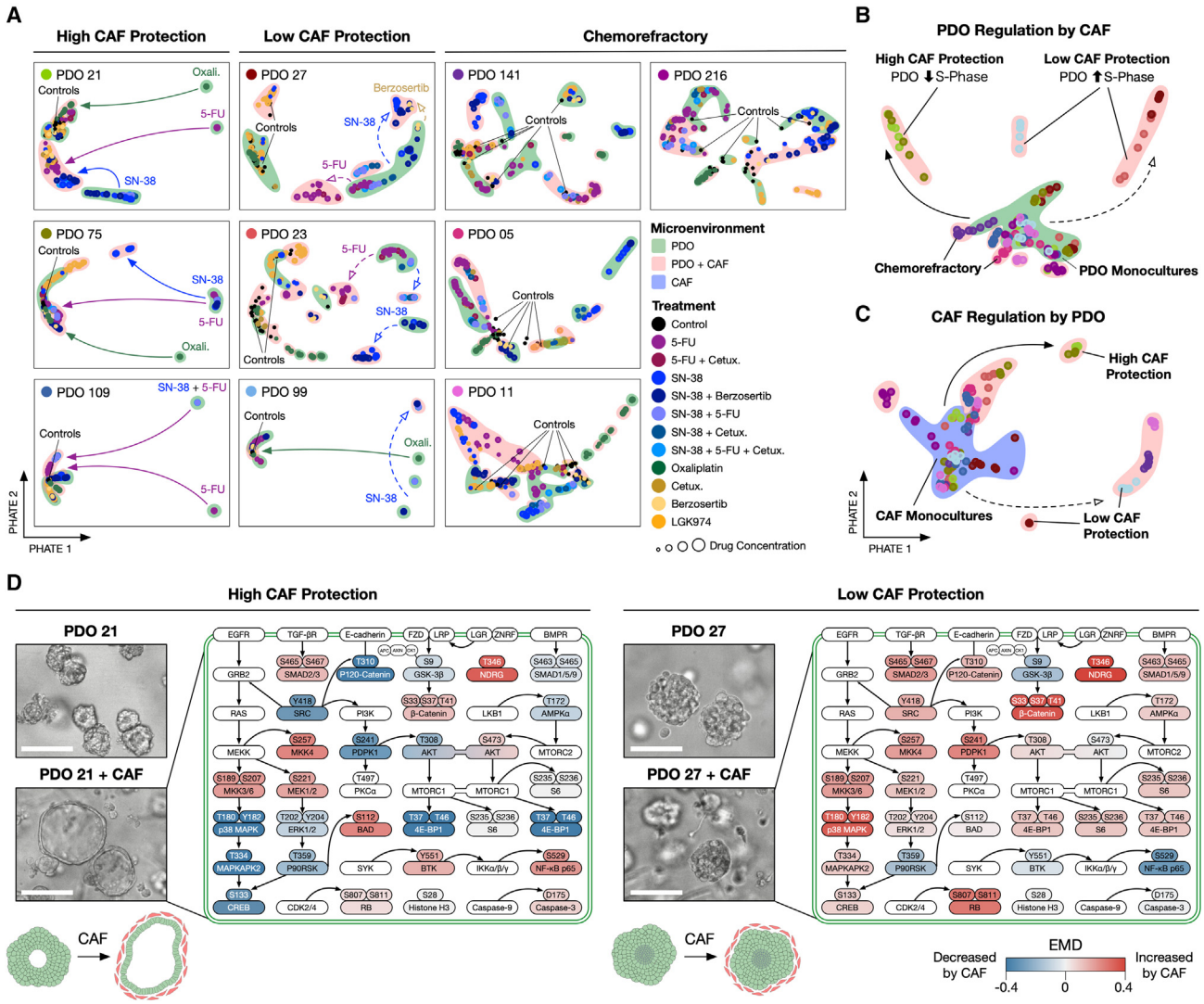

Figure 5. CAFs chemoprotect PDOs by altering PDO PTM signaling

(A) Trellis-PHATE of patient-specific PDO PTM drug responses with or without CAFs illustrates CAFs can protect PDOs from therapy (1,680 PDO-CAF cultures). Dots colored by treatment; outlines colored by microenvironment. Solid arrows refer to full protection; dashed arrows refer to low protection by CAFs.

(B) Alterations of PDO cell state and PTM signaling by CAFs correlates with chemoprotection. Dots correspond to 6 replicates colored by PDO.

(C) Baseline CAF cell state and PTM signaling when co-cultured with PDOs correlates with chemosensitivity protection. Dots correspond to 6 replicates colored by PDO.

(D) CAF regulation of PTM signaling networks in PDO 21 and PDO 27. CAFs down-regulate MAPK and PI3K pathways and up-regulate SMAD, NF-κB, and BAD signaling nodes in protected PDOs. Scale bar, 200 μm.

following drug treatments (Figure 5A). Trellis revealed that CAFs provide varying degrees of chemoprotection in a patient- and drug-specific manner. For example, CAFs completely protect chemosensitive PDOs 21 and 75 from SN-38, 5-FU, and oxaliplatin-induced apoptosis, whereas PDOs 23, 27, and 99 only experience partial chemoprotection (Figure S6A). Chemorefractory PDOs 05, 11, and 141 are largely unaffected by CAFs. This dichotomy suggests CAFs deregulate cancer cells in a patient-specific manner.

We next sought to understand why CAFs have such different patient-specific regulations of PDO drug response. Chemosensitive PDOs 21 and 75 are highly proliferative in monoculture but reduce cell-cycle activity when co-cultured with CAFs (Figures 5B and S6B). We found that CAFs that protect PDOs also have a distinct PTM signaling profile in co-culture (Figure 5C), suggesting patient-specific reciprocal signaling between PDOs and CAFs occurs during chemoprotection. Crucially, CAFs do not cause protected PDOs to exit the cell cycle, but instead reduce MAPK and PI3K signaling, increase TGF-β, JNK, and NF-κB signaling, and slow PDO S-phase entry—rendering PDOs less vulnerable to chemotherapies (Figure 5D). Notably, these pathways are also cell-intrinsically active in chemorefractory PDOs (Figure 4E), suggesting PTM signaling could represent a general biomarker for drug response. CAFs also dramatically alter the macrostructure of PDOs, with chemoprotected PDOs switching from an enveloped

shape to a cyst-like morphology—indicative of a major cell-fate transition. PDOs that do not benefit from CAF chemoprotection do not experience these morphological shifts. Collectively, we find that CAFs can rapidly regulate PTM signaling networks in PDOs and shift previously chemosensitive cancer cells toward a new chemorefractory cell fate.

CAFs polarize chemoprotected PDOs to a revival colonic stem cell fate

We recently demonstrated that colonic stem cells exist on a continuous plasticity landscape spanning hyper-proliferative colonic stem cells (proCSCs) to slow-cycling revival colonic stem cells (revCSCs).[29] proCSCs have high PI3K and MAPK signaling flux, whereas revCSCs have low PI3K activity and are dependent on fibroblast-derived TGF-β-driven YAP signaling. Given that CAFs can polarize PDOs toward a slow-cycling (Figure S6B), high TGF-β, JNK, and NF-κB, and low MAPK and PI3K signaling state (Figure 5D), we hypothesized that CAF chemoprotection may involve a proCSC-to-revCSC transition.

To test this hypothesis, we performed a multivariate scRNA-seq analysis of PDO 21 (high CAF protection) and PDO 27 (low CAF protection) +/− CAFs (n = 18; Figures 6, S6C, and S6D). In agreement with single-cell PTM signaling analysis, Manifold Enhancement of Latent Dimensions (MELD)[30] analysis revealed CAFs have patient-specific effects on PDOs. We found CAFs polarize PDO 21 toward a new cell fate not found in cancer cells alone (Figure 6A), whereas CAFs have little effect on PDO 27 (Figure 6B).

Chemosensitive PDO 21 alone is enriched for a classical proCSC gene signature (*EPHB2*$^+$, *OLFM4*$^+$, and *MKI67*$^+$; Figure 6C) with minimal differentiation into enteroendocrine cells (Figures S6E–S6G). By contrast, PDO 21 + CAFs are polarized to revCSCs (*ANXA1*$^+$, *SOX9*$^+$, *ITGA2*$^+$, *CLDN4*$^+$, and *YAP1*$^+$; Figure 6D). PDO 27 contains a mixture of proCSCs and revCSCs that are not regulated by CAFs (Figure S6H). It has recently been shown that CRC cells can escape chemotherapy by differentiating toward a slow-cycling "diapause"[31] or fetal/revival stem cell fate[32]—although the processes driving this plasticity are unclear. Our results suggest that intercellular CAF signaling can drive the proCSC-to-revCSC cell-fate transition in a patient-specific manner to protect cancer cells from chemotherapies (Figures 6E, S6F, and S6G).

Mechanistic understanding of drug responses by single-cell screening could identify opportunities to rationally re-sensitize refractory PDOs.[33] For example, mass cytometry revealed that CAFs protect chemosensitive PDOs—not by reducing on-target S-phase blockage or DNA damage (Figure S6I), but by polarizing cancer cells toward a slow-cycling, high TGF-β, JNK, and NF-κB, and low MAPK and PI3K signaling state (Figures 6F–6H, S6A, and S6B). These results were consistent across primary CAFs derived from three alternative CRC patients (Figures S6J–S6L), suggesting that PDOs have a patient-specific response to mesenchymal cues. revCSCs are dependent on YAP signaling,[29,32,34] and both scRNA-seq (Figure 6E) and YAP immunofluorescence (Figure 6I) of PDOs confirmed CAFs activate YAP signaling in chemoprotected PDOs.

Using PTM signaling and cell-state insights from single-cell drug screening, we hypothesized that CAFs chemoprotect cancer cells by polarizing them to a YAP-dependent revCSC fate. To test this, we treated PDO 21 + CAF cultures +/− 100 nM Verteporfin (YAP-TEAD complex inhibitor) +/− SN-38 and measured PTM and cell-state responses using TOB*is* mass cytometry. Verteporfin alone did not induce apoptosis in PDOs (Figure 6J), did not increase on-target SN-38-induced DNA damage in PDOs (Figure S7A), and did not regulate CAF cell cycle or apoptosis (Figures S7B and S7C). However, Verteporfin blocked nuclear YAP translocation (Figure S7D) and restored PDOs to an enveloped morphology when in co-culture with CAFs (Figure S7E)—indicating YAP inhibition re-polarized revCSCs back to proCSCs.[29] Crucially, we observed that Verteporfin completely re-sensitized CAF-protected PDOs to SN-38-induced apoptosis (Figure 6J). These results suggest that CAFs can chemoprotect PDOs via a YAP-driven revCSC fate polarization and underscore the value of mechanism-focused single-cell drug screening in overcoming therapy resistance.

Collectively, single-cell PDO-CAF drug screening revealed that CRC drug responses are patient-specific and closely align with pre-treatment cancer cell PTM signaling. Chemosensitive PDOs have high PI3K and MAPK signaling flux and mitotic entry (indicative of proCSCs), whereas chemorefractory PDOs demonstrate high TGF-β, JNK, and NF-κB signaling and low cell-cycle activity (similar to revCSCs). Crucially, CAFs can polarize mitotic proCSC cancer cells to a slow-cycling, drug-tolerant revCSC fate in a patient-specific manner. These results support a CRC drug sensitivity model whereby mitotic proCSC cancer cells retain high stemness but are vulnerable to anti-mitotic chemotherapies (Figure 7A). By contrast, CAFs can polarize cancer cells toward a revCSC fate that also retains high multi-potency, but they are chemorefractory due to their low mitotic PTM signaling (Figure 7B). By combining high stemness with low cell-cycle activity, revCSCs are potent drug-tolerant persister cells that have the potential to repopulate tumors following chemotherapies.[32] Given the relative abundance of revCSC-like cells *in vivo,*[35] our results suggest targeting CAF-induced proCSC-to-revCSC plasticity could improve chemotherapy responses in CRC.

DISCUSSION

PDOs have been widely proposed as personalized avatars of patient-specific drug responses.[36] However, bulk screening technologies have limited previous studies to PDO monocultures alone and provide no mechanistic insight into PDO drug response.[13] Using highly multiplexed single-cell PTM profiling by TOB*is* mass cytometry and tree-based treatment effect analysis by Trellis, we demonstrate that PDO drug responses are patient-specific and reveal that CAFs regulate PDO PTM signaling and cell fate to alter chemosensitivity. PDO-CAF interactions are also patient-specific, with CAFs both stimulating and repressing PTM signaling, cell-cycle activity, and cell-fate plasticity in a patient-specific manner. Crucially, we demonstrate mechanistic profiling of patient-specific drug responses can be used to re-sensitize CAF-protected PDOs.

Unlike static diagnostic metrics (e.g., pharmacogenomics) that have failed to substantially advance precision oncology,[36] PDOs are functional biopsies that can be experimentally tested

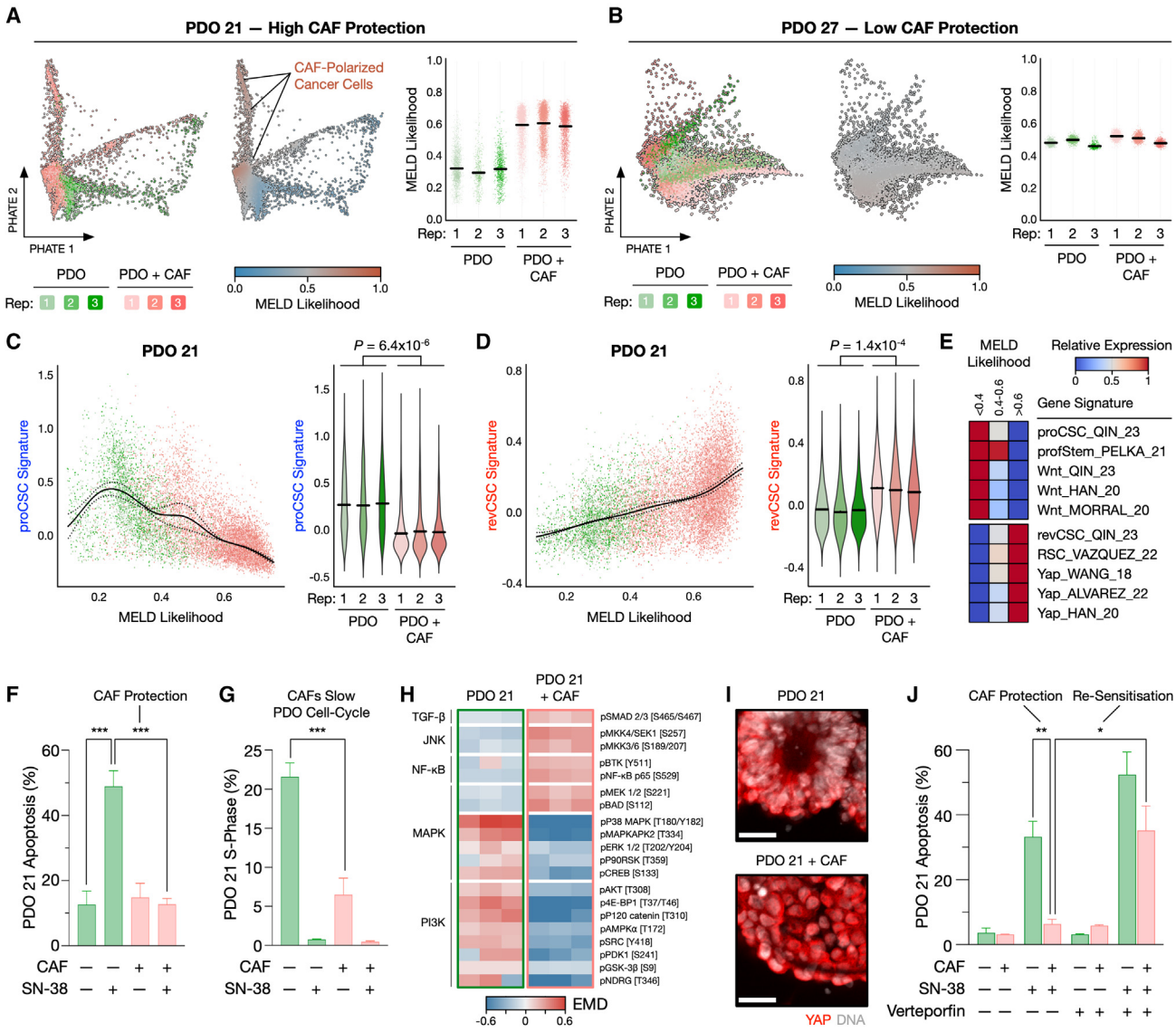

Figure 6. CAFs polarize chemoprotected PDOs to a revival stem cell fate

(A and B) Single-cell PHATE and MELD scores of (A) PDO 21 and (B) PDO 27 +/− CAFs scRNA-seq.

(C) Single-cell PDO 21 proCSC gene signature ranked by MELD score and colored by experimental condition. Mean value of a linear generalized additive model (GAM) for each replicate, unpaired *t* test.

(D) Single-cell PDO 21 revCSC gene signature ranked by MELD score and colored by experimental condition.

(E) Mean relative expression in group for proCSCs, revCSCs, and Wnt and Yap gene signatures per MELD group.

(F) CAFs protect PDOs from SN-38-induced apoptosis.

(G) CAFs slow PDO S-phase entry, and PDOs experience on-target S-phase blockage by SN-38 irrespective of CAFs.

(H) EMD heatmap of PTMs in PDO 21 +/− CAFs demonstrate CAFs regulate PDO PTM signaling.

(I) CAFs induce nuclear translocation of YAP (red) to PDO nucleus (white). Scale bar, 25 μm.

(J) 100 nM Verteporfin re-sensitizes CAF-protected PDOs to SN-38-induced apoptosis. Unpaired *t* test, *** < 0.0001, ** < 0.001, * < 0.01.

See also Figures S6 and S7.

to reveal patient-specific drug responses alongside clinical care in real time.[37–39] However, recent studies have suggested PDOs alone are not sufficient to biomimetically predict drug response. For example, only 20% of monoculture drug combination "hits" could be validated in *ex vivo* organotypic CRC tumors containing a TME,[37] and growth factor regulation of PDO cell state can change organoid drug responses.[40] In agreement with a recent bulk analysis of autologous PDOs and CAFs,[41] our results reveal that PDO-CAF interactions are a source of functional inter-tumor heterogeneity and that the role of CAFs should not be generalized. Given that cell-extrinsic signals can have dramatic effects on drug performance, we propose TME cells should be included

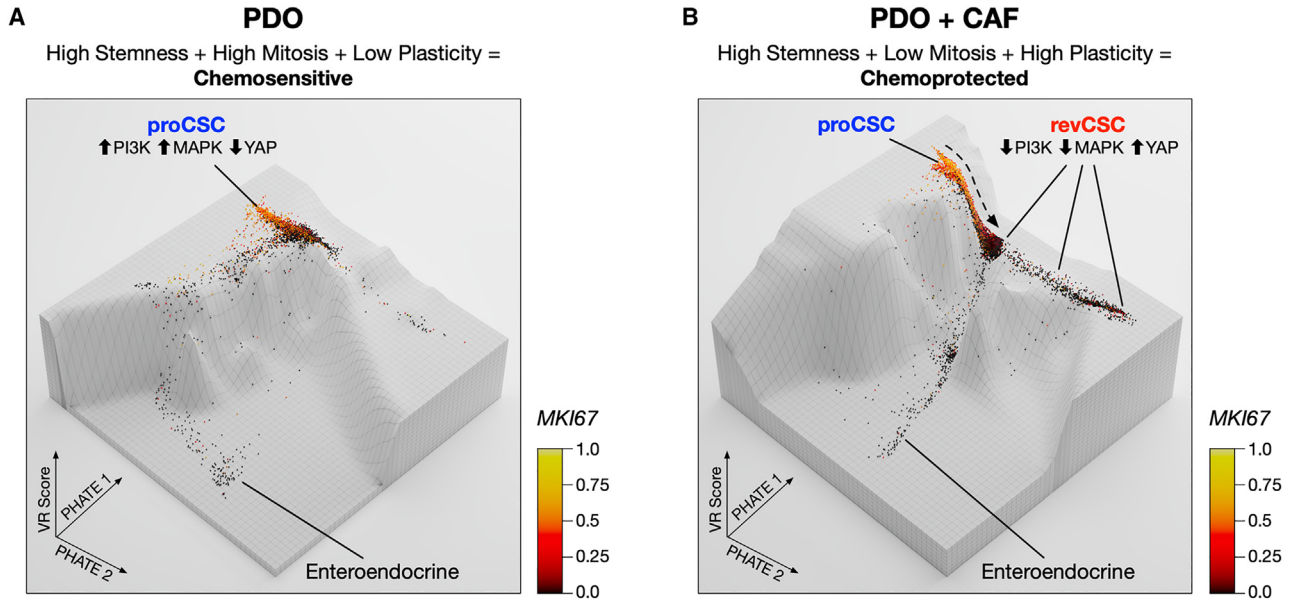

Figure 7. CAF-induced revCSC polarization model

(A) VR landscape model of PDO 21 scRNA-seq. proCSC cancer cells retain high multipotency (CCAT) and high cell-cycle activity (*MKI67*$^{+}$) with minimal differentiation into enteroendocrine cells.

(B) VR landscape model of PDO 21 + CAF scRNA-seq. CAFs increase PDO plasticity to polarize proCSCs toward revCSCs that retain high multipotency but have low cell-cycle activity (*MKI67*$^{-}$), enabling revCSCs to escape chemotherapy.

in future studies evaluating PDOs as personalized functional biopsies.

Phenotypic plasticity is an emerging hallmark of cancer,[42] and therapeutic targeting of cancer-specific cell states is a growing area of cancer research.[43,44] As stem-cell-driven model systems, PDOs are capable of rapid differentiation[8] and are therefore well-suited to studying drug- or TME-induced cancer cell plasticity. We observed that PTM cell state (not MSI/MSS status, tumor stage, anatomical location, or genotype) aligned with patient-specific drug response (Figures 4C, 4D, and S5) and found CAFs can polarize PDOs toward a revCSC-like fate to protect PDOs from clinical therapies. A recent survey of CRC tumors concluded phenotypic variance is largely driven by transcriptional changes rather than genotype,[45] and work in pancreatic ductal adenocarcinoma has demonstrated that PDO transcriptional profiles, not genotype, correlate with drug response.[46] Moreover, recent studies of oncogenic[47] and kinase[48] activity suggest cancer cell signaling flux predicts patient survival better than genotype. Taken with our observations, mounting evidence suggests metrics that more closely describe cancer cell state such as transcription and PTM signaling predict patient-specific drug responses more accurately than genomic profiles or clinical staging.

In contrast to traditional live/dead drug screens, TOB*is* mass cytometry reveals molecular insights into PDO drug responses. We observed PDOs frequently experience on-target drug responses (83%), but only a subset of PDOs enter drug-induced apoptosis (40%). This suggests chemorefractory PDOs do not translate cytostatic and genotoxic stress into apoptosis. Single-cell PTM profiling further revealed CAFs chemoprotect PDOs by shifting cancer cells into a slow-cycling revCSC fate. We used this mechanistic insight to re-sensitize PDOs by blocking revCSC activation via YAP. Given that drug synergy is rare when using unbiased screens,[49] our study suggests mechanism-focused screening could be used to rapidly identify rational drug synergies to re-sensitize refractory cancers.

The advent of high-dimensional single-cell technologies such as mass cytometry and scRNA-seq provides new opportunities to study heterogeneous drug response mechanisms beyond simple viability scores.[13] However, high-dimensional drug screening data are challenging to interpret—with existing tools designed to analyze dozens, not thousands, of samples. Trellis overcomes this scalability bottleneck by distributing single-cell data across a tree domain, enabling the EMD between thousands of single-cell samples to be computed rapidly. While we use cell-state branches to sensitize Trellis results toward canonical on-target anti-cancer drug responses, alternative decision trees could in theory be designed to enrich for PTM signaling hierarchies (e.g., for kinase inhibitor screens) or cell-type hierarchies (e.g., in immune profiling) (Figure S2D). Trellis' scalability is independent of supervening branches, providing a flexible platform for future single-cell screening applications.

In summary, we demonstrate that highly multiplexed single-cell PTM profiling by TOB*is* mass cytometry and tree-based treatment effect analysis by Trellis can reveal patient-specific drug responses in thousands of PDO-CAF cultures. CAFs can regulate PDO drug response by polarizing proCSC cancer cells to a revCSC fate in a patient-specific manner, and PTM signaling

insights can be used to overcome CAF protection. We propose single-cell PTM analysis as a powerful alternative to traditional bulk viability measurements and suggest TME cells should be considered in future precision medicine models.

Limitations of the study

This study used PDOs from the Human Cancer Models Initiative (https://www.cancer.gov/ccg/research/functional-genomics/hcmi) where stromal cells were not collected, so it was not possible to study autologous CAF-PDO communication. While we observe that CAF chemoprotection is common to all CAF lines tested, ideally, future TME models should incorporate autologously paired TME cells.[41] The mass cytometry antibody panel used in this study only targets PTM signaling, cell state, and DNA-damage response, so it could not easily detect cell-fate transitions at scale. Given the emerging importance of cell-fate plasticity in cancer drug resistance, future screening panels should incorporate plasticity markers to detect cell-fate transitions across large PDO cohorts.

STAR★METHODS

Detailed methods are provided in the online version of this paper and include the following:

- KEY RESOURCES TABLE
- RESOURCE AVAILABILITY
  - Lead contact
  - Materials availability
  - Data and code availability
- EXPERIMENTAL MODEL AND SUBJECT DETAILS
  - CRC PDO and CRC CAF culture
  - PDO-CAF drug treatments
  - PDO-CAF sample preparation for scRNA-seq
- METHOD DETAILS
  - PDO-CAF TOB*is* mass cytometry
  - Immunofluorescence microscopy
  - scRNA-seq library, sequencing, and alignment
- QUANTIFICATION AND STATISTICAL ANALYSIS
  - TOB*is* mass cytometry data preprocessing
  - Background in optimal transport for Trellis
  - The Wasserstein metric as a norm
  - The Wasserstein distance with tree ground distance
  - Unpaired and paired Trellis
  - Constructing trees on single-cell mass cytometry data
  - Trellis given a metric tree
  - Paired Trellis
  - Nearest Trellis neighbors
  - Visualizing Trellis embeddings
  - Parameter robustness
  - Related work and time complexity
  - Single-cell RNA-seq data pre-processing and quality control
  - Single-cell RNA-seq perturbation analysis with MELD
  - Generation of single-cell RNA-seq expression signature scores
  - Single-cell RNA-seq VR landscapes

SUPPLEMENTAL INFORMATION

Supplemental information can be found online at https://doi.org/10.1016/j.cell.2023.11.005.

ACKNOWLEDGMENTS

We are extremely grateful to M. Garnett, H. Francies, and the Cell Model Network UK for sharing CRC PDOs and O. De Wever for providing CRC CAFs. We thank the UCL/UCLH Biobank for Studying Health and Disease for the provision of CRC CAFs. We thank Y. Guo, K. Boustani, and G. Morrow from the UCL CI Flow-Core for mass cytometry support. This work was supported by Cancer Research UK (C60693/A23783), the Cancer Research UK City of London Centre (C7893/A26233), the UCLH Biomedical Research Centre (BRC422), the Rosetrees Trust (M872/A2292), the Yale-UCL Collaborative Student Exchange Programme, the NIH (R01GM135929/R01GM130847), the NSF Career (2047856), the Chan Zuckerberg Initiative (CZF2019-182702/CZF2019-002440), and the Sloan Fellowship (FG-2021-15883).

AUTHOR CONTRIBUTIONS

M.R.Z. designed the study, performed all PDO-CAF TOB*is* mass cytometry experiments, analyzed the data, and wrote the paper. A.T. conceived and developed Trellis, analyzed the data, and wrote the paper. J.O. and R.O. performed PDO-CAF SPLiT-seq analysis. J.S. conjugated mass cytometry antibodies and developed TOB*is* barcodes. P.V., C.N., and X.Q. provided PDO and CAF support. F.C.R. analyzed the data. J.C. modeled VR landscapes. D.H. provided chemotherapies and oversaw the project. S.K. conceived and oversaw Trellis and wrote the paper. C.J.T. designed the study, analyzed the data, and wrote the paper.

DECLARATION OF INTERESTS

The authors declare no competing interests.

INCLUSION AND DIVERSITY

We support inclusive, diverse, and equitable conduct of research.

Received: January 7, 2023
Revised: July 27, 2023
Accepted: November 2, 2023
Published: December 7, 2023

REFERENCES

1. Tape, C.J. (2017). The heterocellular emergence of colorectal cancer. Trends Cancer *3*, 79–88.
2. Xi, Y., and Xu, P. (2021). Global colorectal cancer burden in 2020 and projections to 2040. Transl. Oncol. *14*, 101174.
3. Grady, W.M., and Carethers, J.M. (2008). Genomic and epigenetic instability in colorectal cancer pathogenesis. Gastroenterology *135*, 1079–1099.
4. Sahai, E., Astsaturov, I., Cukierman, E., DeNardo, D.G., Egeblad, M., Evans, R.M., Fearon, D., Greten, F.R., Hingorani, S.R., Hunter, T., et al. (2020). A framework for advancing our understanding of cancer-associated fibroblasts. Nat. Rev. Cancer *20*, 174–186.
5. Calon, A., Lonardo, E., Berenguer-Llergo, A., Espinet, E., Hernando-Momblona, X., Iglesias, M., Sevillano, M., Palomo-Ponce, S., Tauriello, D.V.F., Byrom, D., et al. (2015). Stromal gene expression defines poor-prognosis subtypes in colorectal cancer. Nat. Genet. *47*, 320–329.
6. Woolston, A., Khan, K., Spain, G., Barber, L.J., Griffiths, B., Gonzalez-Exposito, R., Hornsteiner, L., Punta, M., Patil, Y., Newey, A., et al. (2019). Genomic and transcriptomic determinants of therapy resistance and immune landscape evolution during anti-egfr treatment in colorectal cancer. Cancer Cell *36*, 35–50.e9.

7. Nicolas, A.M., Pesic, M., Engel, E., Ziegler, P.K., Diefenhardt, M., Kennel, K.B., Buettner, F., Conche, C., Petrocelli, V., Elwakeel, E., et al. (2022). Inflammatory fibroblasts mediate resistance to neoadjuvant therapy in rectal cancer. Cancer Cell *40*, 168–184.e13.
8. Clevers, H. (2016). Modeling development and disease with organoids. Cell *165*, 1586–1597.
9. Vlachogiannis, G., Hedayat, S., Vatsiou, A., Jamin, Y., Fernández-Mateos, J., Khan, K., Lampis, A., Eason, K., Huntingford, I., Burke, R., et al. (2018). Patient-derived organoids model treatment response of metastatic gastrointestinal cancers. Science *359*, 920–926.
10. Letai, A., Bhola, P., and Welm, A.L. (2022). Functional precision oncology: Testing tumors with drugs to identify vulnerabilities and novel combinations. Cancer Cell *40*, 26–35.
11. Yuki, K., Cheng, N., Nakano, M., and Kuo, C.J. (2020). Organoid models of tumor immunology. Trends Immunol. *41*, 652–664.
12. van de Wetering, M., Francies, H.E., Francis, J.M., Bounova, G., Iorio, F., Pronk, A., van Houdt, W., van Gorp, J., Taylor-Weiner, A., Kester, L., et al. (2015). Prospective derivation of a living organoid biobank of colorectal cancer patients. Cell *161*, 933–945.
13. Qin, X., and Tape, C.J. (2021). Deciphering organoids: High-dimensional analysis of biomimetic cultures. Trends Biotechnol. *39*, 774–787.
14. Qin, X., Sufi, J., Vlckova, P., Kyriakidou, P., Acton, S.E., Li, V.S.W., Nitz, M., and Tape, C.J. (2020). Cell-type-specific signaling networks in heterocellular organoids. Nat. Methods *17*, 335–342.
15. Sufi, J., Qin, X., Rodriguez, F.C., Bu, Y.J., Vlckova, P., Zapatero, M.R., Nitz, M., and Tape, C.J. (2021). Multiplexed single-cell analysis of organoid signaling networks. Nat. Protoc. *16*, 4897–4918.
16. De Vlieghere, E., Gremonprez, F., Verset, L., Mariën, L., Jones, C.J., De Craene, B., Berx, G., Descamps, B., Vanhove, C., Remon, J.P., et al. (2015). Tumor-environment biomimetics delay peritoneal metastasis formation by deceiving and redirecting disseminated cancer cells. Biomaterials *54*, 148–157.
17. De Jaeghere, E., De Vlieghere, E., Van Hoorick, J., Van Vlierberghe, S., Wagemans, G., Pieters, L., Melsens, E., Praet, M., Van Dorpe, J., Boone, M.N., et al. (2018). Heterocellular 3d scaffolds as biomimetic to recapitulate the tumor microenvironment of peritoneal metastases in vitro and in vivo. Biomaterials *158*, 95–105.
18. Middleton, M.R., Dean, E., Evans, T.R.J., Shapiro, G.I., Pollard, J., Hendriks, B.S., Falk, M., Diaz-Padilla, I., and Plummer, R. (2021). Phase 1 study of the atr inhibitor berzosertib (formerly m6620, vx-970) combined with gemcitabine +/- cisplatin in patients with advanced solid tumours. Br. J. Cancer *125*, 510–519.
19. Zunder, E.R., Finck, R., Behbehani, G.K., Amir, E.A.D., Krishnaswamy, S., Gonzalez, V.D., Lorang, C.G., Bjornson, Z., Spitzer, M.H., Bodenmiller, B., et al. (2015). Palladium-based mass tag cell barcoding with a doublet-filtering scheme and single-cell deconvolution algorithm. Nat. Protoc. *10*, 316–333.
20. Villani, C. (2009). Optimal Transport: Old and New (Springer).
21. Chen, W.S., Zivanovic, N., van Dijk, D., Wolf, G., Bodenmiller, B., and Krishnaswamy, S. (2020). Uncovering axes of variation among single-cell cancer specimens. Nat. Methods *17*, 302–310.
22. Tong, A., Huguet, G., Natik, A., MacDonald, K., Kuchroo, M., Coifman, R., Wolf, G., and Krishnaswamy, S. (2021). Diffusion Earth Mover's Distance and Distribution Embeddings. In Proceedings of the 38th International Conference on Machine Learning, *139* (PMLR), pp. 10336–10346.
23. Tong, A., Huguet, G., Shung, D., Natik, A., Kuchroo, M., Lajoie, G., Wolf, G., and Krishnaswamy, S. (2022). Embedding Signals on Knowledge Graphs with Unbalanced Diffusion Earth Mover's Distance (ICASSP).
24. Pommier, Y. (2013). Drugging topoisomerases: lessons and challenges. ACS Chem. Biol. *8*, 82–95.
25. Santi, D.V., McHenry, C.S., and Sommer, H. (1974). Mechanism of interaction of thymidylate synthetase with 5-fluorodeoxyuridylate. Biochemistry *13*, 471–481.
26. Bruno, P.M., Liu, Y., Park, G.Y., Murai, J., Koch, C.E., Eisen, T.J., Pritchard, J.R., Pommier, Y., Lippard, S.J., and Hemann, M.T. (2017). A subset of platinum-containing chemotherapeutic agents kills cells by inducing ribosome biogenesis stress. Nat. Med. *23*, 461–471.
27. Behbehani, G.K., Bendall, S.C., Clutter, M.R., Fantl, W.J., and Nolan, G.P. (2012). Single-cell mass cytometry adapted to measurements of the cell cycle. Cytometry A. *81*, 552–566.
28. Rapsomaniki, M.A., Lun, X.K., Woerner, S., Laumanns, M., Bodenmiller, B., and Martínez, M.R. (2018). Cellcycletracer accounts for cell cycle and volume in mass cytometry data. Nat. Commun. *9*, 632.
29. Qin, X., Cardoso Rodriguez, F., Sufi, J., Vlckova, P., Claus, J., and Tape, C.J. (2023). An oncogenic phenoscape of colonic stem cell polarisation. Cell *186*. https://doi.org/10.1016/j.cell.2023.11.004.
30. Burkhardt, D.B., Stanley, J.S., 3rd, Tong, A., Perdigoto, A.L., Gigante, S.A., Herold, K.C., Wolf, G., Giraldez, A.J., van Dijk, D., Krishnaswamy, S., and Krishnaswamy, S. (2021). Quantifying the effect of experimental perturbations at single-cell resolution. Nat. Biotechnol. *39*, 619–629.
31. Rehman, S.K., Haynes, J., Collignon, E., Brown, K.R., Wang, Y., Nixon, A.M.L., Bruce, J.P., Wintersinger, J.A., Singh Mer, A., Lo, E.B.L., et al. (2021). Colorectal cancer cells enter a diapause-like dtp state to survive chemotherapy. Cell *184*, 226–242.e21.
32. Alvarez-Varela, A., Novellasdemunt, L., Barriga, F.M., Hernando-Momblona, X., Canellas-Socias, A., Cano-Crespo, S., Sevillano, M., Cortina, C., Stork, D., Morral, C., et al. (2022). Mex3a marks drug-tolerant persister colorectal cancer cells that mediate relapse after chemotherapy. Nat Cancer *3*, 1052–1070.
33. Jin, H., Wang, L., and Bernards, R. (2023). Rational combinations of targeted cancer therapies: background, advances and challenges. Nat. Rev. Drug Discov. *22*, 213–234.
34. Yui, S., Azzolin, L., Maimets, M., Pedersen, M.T., Fordham, R.P., Hansen, S.L., Larsen, H.L., Guiu, J., Alves, M.R.P., Rundsten, C.F., et al. (2018). Yap/taz-dependent reprogramming of colonic epithelium links ecm remodeling to tissue regeneration. Cell Stem Cell *22*, 35–49.e7.
35. Vasquez, E.G., Nasreddin, N., Valbuena, G.N., Mulholland, E.J., Belnoue-Davis, H.L., Eggington, H.R., Schenck, R.O., Wouters, V.M., Wirapati, P., Gilroy, K., et al. (2022). Dynamic and adaptive cancer stem cell population admixture in colorectal neoplasia. Cell Stem Cell *29*, 1213–1228.e8.
36. Veninga, V., and Voest, E.E. (2021). Tumor organoids: Opportunities and challenges to guide precision medicine. Cancer Cell *39*, 1190–1201.
37. Gavert, N., Zwang, Y., Weiser, R., Greenberg, O., Halperin, S., Jacobi, O., Mallel, G., Sandler, O., Berger, A.J., Stossel, E., et al. (2022). Ex vivo organotypic cultures for synergistic therapy prioritization identify patient-specific responses to combined mek and src inhibition in colorectal cancer. Nat. Cancer *3*, 219–231.
38. Pauli, C., Hopkins, B.D., Prandi, D., Shaw, R., Fedrizzi, T., Sboner, A., Sailer, V., Augello, M., Puca, L., Rosati, R., et al. (2017). Personalized in vitro and in vivo cancer models to guide precision medicine. Cancer Discov. *7*, 462–477.
39. Guillen, K.P., Fujita, M., Butterfield, A.J., Scherer, S.D., Bailey, M.H., Chu, Z., DeRose, Y.S., Zhao, L., Cortes-Sanchez, E., Yang, C.H., et al. (2022). A human breast cancer-derived xenograft and organoid platform for drug discovery and precision oncology. Nat. Cancer *3*, 232–250.
40. Raghavan, S., Winter, P.S., Navia, A.W., Williams, H.L., DenAdel, A., Lowder, K.E., Galvez-Reyes, J., Kalekar, R.L., Mulugeta, N., Kapner, K.S., et al. (2021). Microenvironment drives cell state, plasticity, and drug response in pancreatic cancer. Cell *184*, 6119–6137.e26.
41. Farin, H.F., Mosa, M.H., Ndreshkjana, B., Grebbin, B.M., Ritter, B., Menche, C., Kennel, K.B., Ziegler, P.K., Szabó, L., Bollrath, J., et al. (2023). Colorectal cancer organoid–stroma biobank allows subtype-specific assessment of individualized therapy responses. Can. Discov. *13*, 2192–2211.
42. Hanahan, D. (2022). Hallmarks of cancer: New dimensions. Cancer Discov. *12*, 31–46.

43. Burkhardt, D.B., San Juan, B.P., Lock, J.G., Krishnaswamy, S., and Chaffer, C.L. (2022). Mapping phenotypic plasticity upon the cancer cell state landscape using manifold learning. Cancer Discov. *12*, 1847–1859.

44. Chan, J.M., Zaidi, S., Love, J.R., Zhao, J.L., Setty, M., Wadosky, K.M., Gopalan, A., Choo, Z.N., Persad, S., Choi, J., et al. (2022). Lineage plasticity in prostate cancer depends on jak/stat inflammatory signaling. Science *377*, 1180–e.

45. Househam, J., Heide, T., Cresswell, G.D., Spiteri, I., Kimberley, C., Zapata, L., Lynn, C., James, C., Mossner, M., Fernandez-Mateos, J., et al. (2022). Phenotypic plasticity and genetic control in colorectal cancer evolution. Nature *611*, 744–753.

46. Tiriac, H., Belleau, P., Engle, D.D., Plenker, D., Deschênes, A., Somerville, T.D.D., Froeling, F.E.M., Burkhart, R.A., Denroche, R.E., Jang, G.H., et al. (2018). Organoid profiling identifies common responders to chemotherapy in pancreatic cancer. Cancer Discov. *8*, 1112–1129.

47. East, P., Kelly, G.P., Biswas, D., Marani, M., Hancock, D.C., Creasy, T., Sachsenmeier, K., Swanton, C., TRACERx consortium, Downward, J., and de Carné Trécesson, S. (2022). Ras oncogenic activity predicts response to chemotherapy and outcome in lung adenocarcinoma. Nat. Commun. *13*, 5632.

48. Sousa, A., Dugourd, A., Memon, D., Petursson, B., Petsalaki, E., Saez-Rodriguez, J., and Beltrao, P. (2023). Pan-cancer landscape of protein activities identifies drivers of signalling dysregulation and patient survival. Mol. Syst. Biol. *19*, e10631.

49. Jaaks, P., Coker, E.A., Vis, D.J., Edwards, O., Carpenter, E.F., Leto, S.M., Dwane, L., Sassi, F., Lightfoot, H., Barthorpe, S., et al. (2022). Effective drug combinations in breast, colon and pancreatic cancer cells. Nature *603*, 166–173.

50. Moon, K.R., van Dijk, D., Wang, Z., Gigante, S., Burkhardt, D.B., Chen, W.S., Yim, K., Elzen, A.v.d., Hirn, M.J., Coifman, R.R., et al. (2019). Visualizing structure and transitions in high-dimensional biological data. Nat. Biotechnol. *37*, 1482–1492.

51. Wolf, F.A., Angerer, P., and Theis, F.J. (2018). SCANPY: Large-scale single-cell gene expression data analysis. Genome Biol. *19*, 15.

52. Parekh, S., Ziegenhain, C., Vieth, B., Enard, W., and Hellmann, I. (2018). zUMIs - A fast and flexible pipeline to process RNA sequencing data with UMIs. GigaScience *7*, giy059.

53. Dobin, A., Davis, C.A., Schlesinger, F., Drenkow, J., Zaleski, C., Jha, S., Batut, P., Chaisson, M., and Gingeras, T.R. (2013). STAR: ultrafast universal RNA-seq aligner. Bioinformatics *29*, 15–21.

54. Takahashi, Y., Sato, S., Kurashima, Y., Yamamoto, T., Kurokawa, S., Yuki, Y., Takemura, N., Uematsu, S., Lai, C.-Y., Otsu, M., et al. (2018). A Refined Culture System for Human Induced Pluripotent Stem Cell-Derived Intestinal Epithelial Organoids. Stem Cell Rep. *10*, 314–328.

55. Rosenberg, A.B., Roco, C.M., Muscat, R.A., Kuchina, A., Sample, P., Yao, Z., Graybuck, L.T., Peeler, D.J., Mukherjee, S., Chen, W., et al. (2018). Single-cell profiling of the developing mouse brain and spinal cord with split-pool barcoding. Science *360*, 176–182.

56. Schindelin, J., Arganda-Carreras, I., Frise, E., Kaynig, V., Longair, M., Pietzsch, T., Preibisch, S., Rueden, C., Saalfeld, S., Schmid, B., et al. (2012). Fiji: an open-source platform for biological-image analysis. Nat. Methods *9*, 676–682.

57. Kuchina, A., Brettner, L.M., Paleologu, L., Roco, C.M., Rosenberg, A.B., Carignano, A., Kibler, R., Hirano, M., DePaolo, R.W., and Seelig, G. (2021). Microbial single-cell rna sequencing by split-pool barcoding. Science *371*, eaba5257.

58. Ji, Y., Lotfollahi, M., Wolf, F.A., and Theis, F.J. (2021). Machine learning for perturbational single-cell omics. Cell Syst. *12*, 522–537.

59. Shin, D., Lee, W., Lee, J.H., and Bang, D. (2019). Multiplexed single-cell RNA-seq via transient barcoding for simultaneous expression profiling of various drug perturbations. Sci. Adv. *5*, eaav2249.

60. Dixit, A., Parnas, O., Li, B., Chen, J., Fulco, C.P., Jerby-Arnon, L., Marjanovic, N.D., Dionne, D., Burks, T., Raychowdhury, R., et al. (2016). Perturb-Seq: Dissecting Molecular Circuits with Scalable Single-Cell RNA Profiling of Pooled Genetic Screens. Cell *167*, 1853–1866.e17.

61. Peyré, G., and Cuturi, M. (2019). Computational Optimal Transport. Preprint at arXiv.. https://doi.org/10.48550/arXiv.1803.00567.

62. Chen, S., and Figalli, A. (2017). Partial W2, regularity for optimal transport maps. J. Funct. Anal. *272*, 4588–4605.

63. Caffarelli, L.A. (1992). The Regularity of Mappings with Convex Potential. J. Amer. Math. Soc. *5*, 99–104.

64. Hanin, L.G. (1992). Kantorovich-Rubinstein Norm and Its Application in the Theory of Lipschitz Spaces. Proc. AMS *115*, 345–352.

65. Kuhn, H.W. (1955). The Hungarian method for the assignment problem. Nav. Res. Logist. *2*, 83–97.

66. Cuturi, M. (2013). Sinkhorn Distances: Lightspeed Computation of Optimal Transport. Adv. Neural Inf. Process. Syst. *26*, 2292–2300.

67. Nabavi, S., Schmolze, D., Maitituoheti, M., Malladi, S., and Beck, A.H. (2016). EMDomics: A robust and powerful method for the identification of genes differentially expressed between heterogeneous classes. Bioinformatics *32*, 533–541.

68. Kolouri, S., Zou, Y., and Rohde, G.K. (2016). Sliced Wasserstein Kernels for Probability Distributions. In 2016 IEEE Conference on Computer Vision and Pattern Recognition (CVPR) (IEEE), pp. 5258–5267.

69. Kolouri, S., Nadjahi, K., Simsekli, U., Badeau, R., and Rohde, G. (2019). Generalized Sliced Wasserstein Distances. Adv. Neural Inf. Process. Syst. *32*, 261–272.

70. Indyk, P., and Thaper, N. (2003). Fast image retrieval via embeddings. In 3rd International Workshop on Statistical and Computational Theories of Vision.

71. Le, T., Yamada, M., Fukumizu, K., and Cuturi, M. (2019). Tree-Sliced Variants of Wasserstein Distances. In Advances in Neural Information Processing Systems, *33*.

72. Backurs, A., Dong, Y., Indyk, P., Razenshteyn, I., and Wagner, T. (2020). Scalable Nearest Neighbor Search for Optimal Transport (ICML).

73. Bartal, Y. (1996). Probabilistic Approximation of Metric Spaces and its Algorithmic Applications. In 37th Annual Symposium on Foundations of Computer Science, pp. 184–193.

74. Charikar, M.S. (2002). Similarity Estimation Techniques from Rounding Algorithms (STOC).

75. McInnes, L., Healy, J., and Melville, J. (2018). UMAP: Uniform Manifold Approximation and Projection for Dimension Reduction.

76. van der Maaten, L., and Hinton, G.E. (2008). Visualizing Data using t-SNE. J. Mach. Learn. Res.

77. Aghaeepour, N., Finak, G., FlowCAP Consortium; DREAM Consortium, Hoos, H., Mosmann, T.R., Brinkman, R., Gottardo, R., and Scheuermann, R.H. (2013). Critical assessment of automated flow cytometry data analysis techniques. Nat. Methods *10*, 228–238.

78. von Luxburg, U. (2007). A tutorial on spectral clustering. Stat. Comput. *17*, 395–416.

79. Verschoor, C.P., Lelic, A., Bramson, J.L., and Bowdish, D.M.E. (2015). An Introduction to Automated Flow Cytometry Gating Tools and Their Implementation. Front. Immunol. *6*, 380.

80. Mair, F., Hartmann, F.J., Mrdjen, D., Tosevski, V., Krieg, C., and Becher, B. (2016). The end of gating? An introduction to automated analysis of high dimensional cytometry data: Highlights. Eur. J. Immunol. *46*, 34–43.

81. Cossarizza, A., Chang, H.-D., Radbruch, A., Acs, A., Adam, D., Adam-Klages, S., Agace, W.W., Aghaeepour, N., Akdis, M., Allez, M., et al. (2019). Guidelines for the use of flow cytometry and cell sorting in immunological studies (second edition). Eur. J. Immunol. *49*, 1457–1973.

82. Evans, S.N., and Matsen, F.A. (2012). The phylogenetic Kantorovich-Rubinstein metric for environmental sequence samples. J. R. Stat. Soc. Series B Stat. Methodol. *74*, 569–592.

83. Moon, K.R., Stanley, J.S., Burkhardt, D., van Dijk, D., Wolf, G., and Krishnaswamy, S. (2018). Manifold learning-based methods for analyzing single-cell RNA-sequencing data. Current Opinion in Systems Biology *7*, 36–46.

84. Pedregosa, F., Varoquaux, G., Gramfort, A., Michel, V., Thirion, B., Grisel, O., Blondel, M., Prettenhofer, P., Weiss, R., Dubourg, V., et al. (2011). Scikit-learn: Machine Learning in Python (Machine Learning In Python).

85. Wolock, S.L., Lopez, R., and Klein, A.M. (2019). Scrublet: Computational identification of cell doublets in single-cell transcriptomic data. Cell Syst. *8*, 281–291.e9.

86. Satija, R., Farrell, J.A., Gennert, D., Schier, A.F., and Regev, A. (2015). Spatial reconstruction of single-cell gene expression data. Nat. Biotechnol. *33*, 495–502.

87. Pelka, K., Hofree, M., Chen, J.H., Sarkizova, S., Pirl, J.D., Jorgji, V., Bejnood, A., Dionne, D., Ge, W.H., Xu, K.H., et al. (2021). Spatially organized multicellular immune hubs in human colorectal cancer*184*, pp. 4734–4752.e20.

88. Han, T., Goswami, S., Hu, Y., Tang, F., Zafra, M.P., Murphy, C., Cao, Z., Poirier, J.T., Khurana, E., Elemento, O., et al. (2020). Lineage Reversion Drives WNT Independence in Intestinal Cancer. Cancer Discov. *10*, 1590–1609.

89. Morral, C., Stanisavljevic, J., Hernando-Momblona, X., Mereu, E., Álvarez-Varela, A., Cortina, C., Stork, D., Slebe, F., Turon, G., Whissell, G., et al. (2020). Zonation of Ribosomal DNA Transcription Defines a Stem Cell Hierarchy in Colorectal Cancer. Cell Stem Cell *26*, 845–861.e12.

90. Wang, Y., Xu, X., Maglic, D., Dill, M.T., Mojumdar, K., Ng, P.K.-S., Jeong, K.J., Tsang, Y.H., Moreno, D., Bhavana, V.H., et al. (2018). Comprehensive Molecular Characterization of the Hippo Signaling Pathway in Cancer. Cell Rep. *25*, 1304–1317.e5.

91. Smedley, D., Haider, S., Ballester, B., Holland, R., London, D., Thorisson, G., and Kasprzyk, A. (2009). Biomart–biological queries made easy. BMC Genom. *10*, 22.

92. Servén, D., Brummitt, C., and Abedi, H. (2018). dswah/pygam: v0.8.0.

93. Teschendorff, A.E., and Enver, T. (2017). Single-cell entropy for accurate estimation of differentiation potency from a cell's transcriptome. Nat. Commun. *8*, 15599.

94. Bergen, V., Lange, M., Peidli, S., Wolf, F.A., and Theis, F.J. (2020). Generalizing RNA velocity to transient cell states through dynamical modeling. Nat. Biotechnol. *38*, 1408–1414.

95. Chen, W., Morabito, S.J., Kessenbrock, K., Enver, T., Meyer, K.B., and Teschendorff, A.E. (2019). Single-cell landscape in mammary epithelium reveals bipotent-like cells associated with breast cancer risk and outcome. Commun. Biol. *2*, 1–13.

96. Senra, D., Guisoni, N., and Diambra, L. (2022). ORIGINS: A protein network-based approach to quantify cell pluripotency from scRNA-seq data. MethodsX *9*, 101778.

97. Spitzer, M.H., Gherardini, P.F., Fragiadakis, G.K., Bhattacharya, N., Yuan, R.T., Hotson, A.N., Finck, R., Carmi, Y., Zunder, E.R., Fantl, W.J., et al. (2015). Immunology. an interactive reference framework for modeling a dynamic immune system. Science *349*, 1259425.

STAR★METHODS

KEY RESOURCES TABLE

REAGENT or RESOURCE	SOURCE	IDENTIFIER
Antibodies		
Phospho-Histone H3 [S28]	BioLegend	Cat#641007; Clone: HTA28; RRID: AB_2562851
CD326 (EpCAM) (Hm)	BioLegend	Cat#324229; Clone: 9C4; RRID: AB_2563742
Pan-Cytokeratin (Pan-CK)	BioLegend	Cat#628602; Clone: AE1/AE3; RRID: AB_2616960
CK18	Abcam	Cat#ab668; Clone: C-04; RRID: AB_305647
Phospho-PDK1 [S241]	BD Biosciences	Cat#558395; Clone: J66-653.44.22; RRID: AB_647291
Cleaved-Caspase 3 [D175]	CST	Cat#9579; Clone: D3E9; RRID: AB_10897512
Cleaved-PARP [D214]	CST	Cat#5625BF; Clone: F21-852
Phospho-MKK4/SEK1 [S257]	CST	Cat#4514; Clone: C36C11; RRID: AB_2140946
Phospho-BTK [Y551]	BD Biosciences	Cat#558034; Clone: 24a/BTK; RRID: AB_2067823
Phospho-SRC [Y418]	Thermo	Cat#14-9034-82; Clone: SC1T2M3; RRID: AB_2572916
Phospho-4E-BP1 [T37/46]	CST	Cat#2855; Clone: 236B4; RRID: AB_560835
Phospho-RB [S807/811]	BD Biosciences	Cat#558389; Clone: J112-906; RRID: AB_647295
Phospho-PKCα [T497]	BD Biosciences	Cat#560141; Clone: K14-984; RRID: AB_1645332
Phospho-AKT [T308]	BD Biosciences	Cat#558316; Clone: J1-223.371; RRID: AB_647259
Phospho-CREB [S133]	CST	Cat#9198; Clone: 87G3; RRID: AB_2561044
Phospho-SMAD1 [S463/465] Phospho-SMAD5 [S463/465] Phospho-SMAD9 [S465/467]	CST	Cat#13820; Clone: D5B10; RRID: AB_2493181
Phospho-AKT [S473]	CST	Cat#4060; Clone: D9E; RRID: AB_2315049
Phospho-NF-κB p65 [S529]	BD Biosciences	Cat#558393; Clone: K10-895.12.50; RRID: AB_647284
Phospho-MKK3 [S189]/MKK6 [S207]	CST	Cat#12280; Clone: D8E9; RRID: AB_2797868
Phospho-p38 MAPK [T180/Y182]	CST	Cat#4511; Clone: D3F9; RRID: AB_2139682
Phospho-MAPKAPK2 [T334]	CST	Cat#3007; Clone: 27B7; RRID: AB_490936
Phospho-AMPKα [T172]	CST	Cat#2535; Clone: 40H9; RRID: AB_331250
Phospho-BAD [S112]	CST	Cat#5284; Clone: 40A9; RRID: AB_560884
Phospho-p90RSK [T359]	CST	Cat#8753; Clone: D1E9; RRID: AB_2783561
Phospho-p120-Catenin [T310]	BD Biosciences	Cat#558203; Clone: 22/p120 (pT310); RRID: AB_397057
β-Catenin [Active]	CST	Cat#8814; Clone: D13A1; RRID: AB_11127203

(*Continued on next page*)

Continued

REAGENT or RESOURCE	SOURCE	IDENTIFIER
Phospho-GSK-3β [S9]	CST	Cat#5558; Clone: D85E12; RRID: AB_10013750
Phospho-ERK1/2 [T202/Y204]	BD Biosciences	Cat#612359; Clone: 20A; RRID: AB_399648
Phospho-SMAD2 [S465/467] Phospho-SMAD3 [S423/425]	CST	Cat#8828; Clone: D27F4; RRID: AB_2631089
GFP	eBiosciences	Cat#13-6498-82; Clone: 5F12.4; RRID: AB_11043422
Phospho-MEK1/2 [S221]	CST	Cat#2338; Clone: 166F8; RRID: AB_490903
Phospho-NDRG1 [T346]	CST	Cat#5482; Clone: D98G11; RRID: AB_10693451
Phospho-S6 [S235/236]	CST	Cat#4858; Clone: D57.2.2E; RRID: AB_916156
Phospho-Histone H2A.X [S139]	CST	Cat#80312BF; Clone: D7T2V
Phospho-DNAPK [S2056]	Abcam	Cat#ab174576; Clone: EPR5670
Phospho-CHK1 [S345]	BD Biosciences	Cat#2348BF; Clone: 133D3
CD90 (THY1)	BioLegend	Cat#328102; Clone: 5E10; RRID: AB_940390
Cyclin B1	BD Biosciences	Cat#554179; Clone: GNS-11; RRID: AB_395290
Podoplanin	BioLegend	Cat# 127401; Clone: 8.1.1; RRID:AB_1089186
RFP	eBiosciences	Cat#200-301-379; Clone: 8E5.G7; RRID: AB_2611063
mCherry	Thermofischer	Cat#M11217; Clone: 16D7; RRID: AB_2536611
Geminin	Santa Cruz	Cat#10802-1-AP; Clone: Polyclonal; RRID: AB_2110945
CHGA	Insight Biotechnology	Cat#sc-393941; Clone: C-12; RRID: AB_2801371
Vimentin	BD Biosciences	Cat#5741; Clone: D21H3; RRID: AB_10695459
PLK1	Thermofischer	Ca# 37-7000; Clone: 35-206; RRID: AB_2533335
YAP	CST	Cat#14074; Clone: D8H1X; RRID: AB_2650491
Goat Anti-Mouse IgG (H + L)	Invitrogen	Cat# 15491034
Goat Anti-Rabbit IgG (H + L)	Invitrogen	Cat# 10348502
Chemicals, peptides, and recombinant proteins		
Advanced DMEM F/12	Thermo	Cat# 12634010
Growth Factor Reduced Matrigel	Corning	Cat# 354230
B-27 Supplement	Thermo	Cat# 17504044
N-2 Supplement	Thermo	Cat# 17502048
L-glutamine	Thermo	Cat# 25030081
A83-01	Generon	Cat# 04-0014
SB202190	Avantor	Cat# CAYM1001039910
HEPES	Sigma	Cat# H3375
EGF	Thermo	Cat# PMG8041
Gastrin I	Sigma	Cat# SCP0152
HyClone Penicillin-Streptomycin Solution	Fisher	Cat# SV30010
N-acetyl-L-cysteine	Sigma	Cat# A9165
Nicotinamide	Sigma	Cat# 0636

(*Continued on next page*)

Continued

REAGENT or RESOURCE	SOURCE	IDENTIFIER
Insulin-Transferrin-Selenium-Sodium Pyruvate (ITS-A)	Thermo	Cat# 51300044
Heat Inactivated Fetal Bovine Serum	Thermo	Cat# 10082147
TrypLE™ Express Enzyme	Thermo	Cat# 12604013
Dispase II	Thermo	Cat# 17105041
Recovery™ Cell Culture Freezing Medium	Thermo	Cat# 12648010
^{127}5-Iodo-2′-deoxyuridine (^{127}IdU)	Sigma	Cat# I7125
Protease Inhibitor Cocktail	Sigma	Cat# P8340
PhosSTOP™	Sigma	Cat# 4906845001
^{194}Cisplatin	Standard BioTools	Cat# 201194
^{198}Cisplatin	Standard BioTools	Cat# 201198
Collagenase IV	Thermo	Cat# 17104019
DNase I	Sigma	Cat# DN25
Cell Staining Buffer	Standard BioTools	Cat# 201068
TOB*is* (*9*-choose-*4*)	Sufi et al., 2021[15]	N/A
L-Glutathione	Sigma	Cat# G6529
SN-38	Sigma	Cat# H0165
5-FU	Merck	Cat# F6627
Oxaliplatin	Merck	Cat# O9512
Cetuximab	MedChem Express	Cat# HY-P9905
VX-970	Selleckchem	Cat# S7102
LGK-974	Peprotech	Cat# 1241454
Verteporfin	Cayman Chemical	Cat# CAY17334
PROTECTOR RNASE INHIBITOR, 10 000 U	Sigma/Merck	Cat# 3335402001
SUPERase-In RNase Inhibitor (20 U/uL)	Thermo	Cat# AM2694
Maxima H Minus Reverse Transcriptase (200 U/μL)	Thermo	Cat# EP0753
dNTP Mix (10 mM ea)-100 uL	Thermo	Cat# 18427013
NEB buffer 3.1 10x	NED	Cat# B7203S
T4 DNA Ligase	NED	Cat# M0202L
T4 DNA Ligase reaction buffer 10x	NED	Cat# B0202S
EDTA Solution (BioUltra, for molecular biology, pH 8.0, ∼0.5 M in H2O)	Sigma	Cat# 03690-100ML
Proteinase K	Invitrogen (Thermo)	Cat# AM2546
DiYO™-1 FITC dsDNA stain - 1mg (AAT Bioquest)	Stratech	Cat# 17579
NaCl(5 M), RNase-free (100mL)	Thermo	Cat# AM9760G
SDS	Invitrogen (Thermo)	Cat# 15553027
Tris 1M pH 8.0 RNase-free 100mL	Thermo	Cat# AM9855G
UltraPure 1M Tris-HCl, pH 8.0–1 L	Thermo	Cat# 15568025
"Tween 20 Surfact-Amps Detergent Solution, Formulation: 10% (w/v) aqueous solution of Tween 20, Properties: Nonionic"	Thermo	Cat# 85113
PMSF (Phenylmethylsulfonyl fluoride) peptidase inhibitor	Thermo	Cat# 36978
Dynabeads™ MyOne™ Streptavidin C1	Invitrogen (Thermo)	Cat# 65001
Ficoll PM-400 (20%)	Merck	Cat# F5415-25ML
KAPA HiFi HotStart ReadyMix	KAPA (Roche)	Cat# KK2601
SPRI Kapa Pure Beads	Kapa (Roche)	Cat# KK8000

(*Continued on next page*)

Continued

REAGENT or RESOURCE	SOURCE	IDENTIFIER
Critical commercial assays		
Nextera XT DNA Library Preparation Kit (24 samples)	Illumina	Cat# FC-131-1024
Qubit™ 1X dsDNA HS Assay Kit	Invitrogen (Thermo)	Cat# Q33230
Agilent High Sensitivity DNA Kit	Agilent	Cat# 5067-4626
NovaSeq 6000 S2 Reagent Kit v1.5 (200 cycles)	Ilumina	Cat# 20028315
Deposited data		
Mass cytometry data (raw)	This paper	https://community.cytobank.org/cytobank/projects/1461
Mass cytometry data (processed)	This paper	https://data.mendeley.com/datasets/hc8gxwks3p
scRNA-seq data (raw)	This paper	GEO: GSE239386
scRNA-seq data (processed)	This paper	https://zenodo.org/record/8177571
Experimental models: Organoids		
PDO 5	Sanger Institute	HCM-SANG-0266-C20
PDO 11	Sanger Institute	HCM-SANG-0267-D12
PDO 21	Sanger Institute	HCM-SANG-0270-C20
PDO 23	Sanger Institute	HCM-SANG-0271-D12
PDO 27	Sanger Institute	HCM-SANG-0273-C18
PDO 75	Sanger Institute	HCM-SANG-0278-C20
PDO 99	Sanger Institute	HCM-SANG-0282-C18
PDO 109	Sanger Institute	HCM-SANG-0529-C18
PDO 141	Sanger Institute	HCM-SANG-0284-C18
PDO 216	Sanger Institute	HCM-SANG-0520-C18
Experimental models: Cell lines		
CRC CAFs GFP$^+$	Prof. Olivier de Wever, University of Gent.	N/A
L cells	Shintaro Sato, Research Institute of Microbial Diseases, Osaka University.	N/A
Primary CRC CAFs	UCL Biobank, University College London Hospital.	N/A
Oligonucleotides		
SPLiT-Seq BARCODE SEQUENCES	This paper	Table S4
Software and algorithms		
FIJI	NIH	https://fiji.sc/
Cytobank	Cytobank, Inc.	http://www.cytobank.org
Graphpad Prism 7	GraphPad Software	https://www.graphpad.com/
OmniGraffle Professional 7	The Omni Group	https://www.omnigroup.com/omnigraffle
scprep	Laboratory of Smita Krishnaswamy, Yale University	https://scprep.readthedocs.io/en/stable/
phate	Moon et al.[50]	https://phate.readthedocs.io/en/stable/
Trellis	This paper	https://github.com/KrishnaswamyLab/Trellis
Scanpy	Wolf et al.[51]	https://scanpy.readthedocs.io/en/stable/
Seurat	Laboratory of Rahul Satija, New York Genome Center	https://satijalab.org/seurat/
zUMIs (Version 2.9.7)	Parekh et al.[52]	https://github.com/sdparekh/zUMIs
STAR (Version 2.7.3a)	Dobin et al.[53]	https://github.com/alexdobin/STAR

(*Continued on next page*)

Continued

REAGENT or RESOURCE	SOURCE	IDENTIFIER
Other		
μ-Slides	ibidi	Cat#80826
gentleMACS C-Tube	Miltenyi	Cat#130-096-334
gentleMACS Octo Dissociator (with Heaters)	Miltenyi	Cat#130-096-427
EQ™ Four Element Calibration Beads	Standard BioTools (previously Fluidigm)	Cat#201078
EQ™ Six Element Calibration Beads	Standard BioTools	Cat#201245
Helios Mass-Cytometer	Standard BioTools (previously Fluidigm)	http://cn.fluidigm.com/products/helios
CyTOF XT Mass-Cytometer	Standard BioTools	https://www.standardbio.com/products/instruments/cytof-xt
Illumina NovaSeq 6000	Illumina	https://www.illumina.com/systems/sequencing-platforms/novaseq.html

RESOURCE AVAILABILITY

Lead contact

Further information and requests for resources and reagents should be directed to and will be fulfilled by the lead contact, Christopher J. Tape (c.tape@ucl.ac.uk).

Materials availability

This study did not generate new unique reagents.

Data and code availability

- Single-cell RNA-seq data have been deposited at GEO and are publicly available as of the date of publication. Accession number is listed in the key resources table. Raw and gated mass cytometry data have been deposited at Community Cytobank and are publicly available as of the date of publication. The project URL is listed in the key resources table. Aligned scRNA-seq count matrices, spliced/unspliced RNA count matrices, integrated Seurat objects, and integrated mass cytometry dataframes have been deposited at Mendeley and Zenodo and are publicly available as of the date of publication. DOIs are listed in the key resources table.
- All original code to reproduce figures in the manuscript together with supplemental analysis has been deposited at GitHub and is publicly available as of the date of publication. The repository URL is listed in the key resources table.
- Any additional information required to reanalyse the data reported in this paper is available from the lead contact upon request.

EXPERIMENTAL MODEL AND SUBJECT DETAILS

CRC PDO and CRC CAF culture

CRC PDOs were obtained from the Human Cancer Models Initiative (Sanger Institute, Cambridge, UK)[12] and expanded in 12-well plates (Helena Biosciences 92412T) in x3 25 μL droplets of Growth Factor Reduced Matrigel (Corning 354230) per well with 1 mL of Advanced DMEM F/12 (Thermo 12634010) containing 2 mM L-glutamine (Thermo 25030081), 1 mM N-acetyl-L-cysteine (Sigma A9165), 10 mM HEPES (Sigma H3375), 500 nM A83-01 (Generon 04–0014), 10 μM SB202190 (Avantor CAYM10010399-10), and 1X B-27 Supplement (Thermo 17504044), 1X N-2 Supplement (Thermo 17502048), 50 ng mL^{-1} EGF (Thermo PMG8041), 10 nM Gastrin I (Sigma SCP0152), 10 mM Nicotinamide (Sigma N0636), and 1X HyClone Penicillin-Streptomycin Solution (Fisher SV30010), and conditioned media produced as described in[54] at 5% CO_2, 37°C. PDOs were dissociated into single cells with 1X TripLE Express Enzyme (Gibco 12604013) (incubated at 37°C for 20 min) and passaged every 10 days. L-cells for conditioned media production were obtained from Shintaro Sato (Research Institute of Microbial Diseases, Osaka University, Osaka, Japan). To aid cell-type-specific visualization and gating, CRC PDO were transfected with H2B-RFP (Addgene 26001). CRC CAFs (+GFP) were a kind gift from Prof. Olivier De Wever (University of Gent).[16,17] Primary CAFs were isolated from consented CRC patients at UCLH via the UCL Biobank (HTA Licence: 12055, REC ref. 15/YH/0311). All CAFs were cultured in DMEM (Thermo 11965092) enriched with 10% FBS (Gibco 10082147), and 1X HyClone Penicillin-Streptomycin Solution (Fisher SV30010) at 5% CO_2, 37°C.

PDO-CAF drug treatments

PDOs were dissociated into single cells on day 0, and expanded in 12-well plates in Growth Factor Reduced Matrigel (Corning 354230) with Advanced DMEM F/12 (Thermo 12634010) containing 2 mM L-glutamine (Thermo 25030081), 1 mM N-acetyl-L-cysteine (Sigma

A9165), 10 mM HEPES (Sigma H3375), 1X B-27 Supplement (Thermo 17504044), 1X N-2 Supplement (Thermo 17502048), 50 ng mL^{-1} EGF (Thermo PMG8041), 10 nM Gastrin I (Sigma SCP0152), 10 mM Nicotinamide (Sigma N0636), 500 nM A83-01 (Generon 04–0014), 10 μM SB202190 (Avantor CAYM10010399-10) and 1X HyClone Penicillin-Streptomycin Solution (Fisher SV30010) at 5% CO_2, 37°C for 4 days. On day 5, PDOs were starved in Reduced media (Advanced DMEM F/12 containing only 2 mM L-glutamine, 1 mM N-acetyl-L-cysteine, 10 mM HEPES, 1X B-27 Supplement, 1X N-2 Supplement, 10 mM Nicotinamide, and 1X HyClone-Penicillin Streptomycin Solution) at 5% CO_2, 37°C. In parallel, CAFs were starved in 2% FBS DMEM with 1X Hyclone-Penincillin Streptomycin Solution. PDOs and CAFs were seeded on day 6 in 96-well plates (Helena Biosciences 92696T) in 50 μL Matrigel stacks with 300 μL of reduced media. PDO monocultures are seeded at a density of ~ 1.5 x 10^3 organoids/well, and CAFs at 2.5 x 10^5 cells/well, co-cultures were mixed in Matrigel on ice at the densities described, and seeded together on the plates for polymerization. On day 7, media was replaced with titrated concentrations of SN-38 (Sigma H0165), 5-FU (Merck F6627), Oxaliplatin (Merck O9512), Cetuximab (MedChem Express HY-P9905), VX-970 (Stratech), and LGK-974 (Peprotech 1241454) (Table S2) diluted in Reduced media. On day 8, media was replaced with the corresponding treatments (same as on day 7). After 72 h of co-culture, and 48-h of treatment (day 9), cultures were processed for TOB*is* mass cytometry (see below). Verteporfin (Cambridge Bioscience CAY17334) was used at 100 nM as above and added in the media from the start of the co-cultures, on day 6.

PDO-CAF sample preparation for scRNA-seq

PDO-CAF co-cultures were cultured as described above. After 72 h, organoids were dissociated into single cells using TrypLE (Thermo 12604013) incubated for 10 min at 37°C on a heated orbital shaker at 300 rpm. Sample preparation was then performed based on the SPLiT-seq protocol Rosenberg et al.[55] Briefly, cells were filtered 1-2x through a 35 μM filter until in a single-cell suspension and re-suspended in 1 mL of PBS with 1.25 μL Protectorase RNAse inhibitor (Merck 3335402001) and 2.5 μL Superase RNase inhibitor (Thermo AM2694), which was the standard RNase inhibitor concentration, known as '+RI'. Cells were then fixed in 1% (v/v) ice-cold FA/PBS (Thermo 28906) for 10 min on ice. Cells were then permeabilized in 0.2% Triton X-100 +RI for 3 min on ice. Fixation was quenched with 50 mM Tris-HCL and cells were re-suspended in 0.5x PBS +RI. Cells were counted and 5% (v/v) DMSO was added before aliquoting cells for freezing in a Mr Frosty at −80°C.

METHOD DETAILS

PDO-CAF TOB*is* mass cytometry

PDO-CAF co-cultures were analyzed using the TOB*is* mass cytometry protocol outlined in detail by Sufi and Qin et al., Nature Protocols, 2021.[15] Briefly, following drug treatment, PDO-CAF cultures were incubated with 25 μM (5-Iodo-2′-deoxyuridine) (^{127} IdU) (Fluidigm 201127) at 37°C for 30 min, and 5 min before the end of this incubation, 1X Protease Inhibitor Cocktail (Sigma, P8340) and 1 XPhosSTOP (Sigma 4906845001) are added into the media. After the incubation with ^{127} IdU, protease inhibitors and PhosSTOP, each well is fixed in 4% PFA/PBS (Thermo J19943K2) for 1 h at 37°C. PDO-CAFs were washed with PBS, dead cells were stained using 0.25 μM^{194} Cisplatin (Fluidigm 201194), and PDO-CAFs were barcoded *in situ* with 126-plex (*9-choose-4*) TOB*is* overnight at 4°C. Unbound barcodes were quenched in 2 mM GSH and all PDO-CAFs were pooled. PDO-CAFs were dissociated into single cells using 1 mg mL^{-1} Dispase II (Thermo 17105041), 0.2 mg mL^{-1} Collagenase IV (Thermo 17104019), and 0.2 mg mL^{-1} DNase I (Sigma DN25) in C-Tubes (Miltenyi 130-096-334) via gentleMACS Octo Dissociator with Heaters (Miltenyi 130-096-427). Single PDO and CAF cells were washed in cell staining buffer (CSB) (Fluidigm 201068) and stained with extracellular rare-earth metal conjugated antibodies (Table S3) for 30 min at room temperature. PDO-CAFs were then permeabilized in 0.1% (v/v) Triton X-100/PBS (Sigma T8787), 50% methanol/PBS (Fisher 10675112), and stained with intracellular rare-earth metal conjugated antibodies for 30 min at room temperature. PDO-CAFs were then washed in CSB and antibodies were cross-linked to cells using 1.6% (v/v) FA/PBS for 10 min. PDO-CAFs were incubated in 125 nM^{191} $Ir/^{193}$ Ir DNA intercalator (Fluidigm 201192A) overnight at 4°C. PDO-CAFs were washed, resuspended in 2 mM EDTA (Sigma 03690) in water (Fluidigm 201069), and analyzed using a Helios Mass Cytometer (Fluidigm) fitted with a 'Super Sampler' (Victorian Airships) or CyTOF XT (Fluidigm) at 200–400 events s^{-1}.

Immunofluorescence microscopy

PDOs and CAFs were expanded as explained previously (days 1–5), on day 6, monocultures and co-cultures were seeded in 8-well μ slides (ibidi 80826) in 10 μL of Matrigel. Cells were cultured in 200 μL of base media containing Verteporfin or vehicle control (water) and media was refreshed every 24h with the same concentration of inhibitor or vehicle. On day 9, media was removed and cells were washed with PBS at room temperature for 5 min. Cultures were fixed with 4% PFA/PBS (Thermo J19943K2) for 30 min at 4°C. Cells were washed twice with PBS and permeabilised with 0.2% Triton X-100 (Sigma T8787) in PBS for 30 min at room temperature. Permeabilising solution was removed and cells were incubated in blocking solution, containing PBS with 1% BSA (CST 9998) and 0.3% Triton X-100/PBS for 30 min at room temperature. PBS was removed from the wells and cells were incubated with primary antibodies diluted in blocking solution overnight at 4°C. Cells were washed three times with PBS for 5 min and then stained with secondary antibodies and 4′,6-diamidino-2-phenylindole (DAPI) (Thermo D1306) diluted in blocking solution for 1 h at room temperature, protected from the light. Cells were washed 3 times with PBS for 5 min and once with ddH_2O and mounted with Fluoromount-G mounting medium (Thermo Fisher 00-4958-02). Samples were imaged with a Zeiss LSM880 Confocal Microscope and images were analyzed using FIJI.[56]

Phase-contrast microscopy images were generated using an EVOS FL Base Microscope System.

scRNA-seq library, sequencing, and alignment

The scRNA-seq processing protocol followed the SPLiT-seq protocol[55] with minor modifications to the RT oligos and linker oligos.[57] All oligonucleotides and the layout of the barcoding plates used in the protocol can be found in Table S4, reverse transcription Round 1 oligos 01–96 and ligation linking and blocking oligos BC_0340, BC_0335 and BC_0284 were derived from.[57] All other oligos were derived from.[55] One complete SPLiT-seq experiment was performed for each PDO studied (two independent SPLiT-seq runs total). Briefly, cells were thawed, diluted in 0.5x PBS + RI and 8 μL loaded into 12 μL of RT-mix in the 48-wells of the SPLiT-seq barcode-1 reverse transcription plate and reverse transcription performed with Maxima H Minus Reverse Transcriptase (Fisher Scientific EP0753) as specified in.[55] Cells were then pooled and resuspended into NEB 3.1 Buffer (New England BioLabs B7203S), T4 DNA Ligase (New England BioLabs M0202L) and Ligase Buffer (New England BioLabs B0202S). Cell-ligase reaction mixture (40 μL) was then loaded into the 96-well barcode-2 ligation plate (10 μL) and ligation was carried out in a thermocycler for 30 min at 37°C. The round 2 blocking solution (10 μL) was added to each well of the barcode-2 plate and incubated in a thermocycler for 30 min at 37°C. Cells were then pooled and filtered through a 40 μM filter into a basin and 100 μL T4 DNA ligase was added. 50 μL Cell-ligase reaction mixture was then loaded into the 96-well barcode-3 ligation plate (10 μL) and ligation was carried out in a thermocycler for 30 min at 37°C. The round 3 blocking solution (20 μL) was added to each well of the barcode-3 plate and cells were then pooled into a new basin and filtered through a 40 μM into a 15 mL tube on ice. Cells were then washed with 4 mL 0.1% Triton X-100 solution and resuspended in 50 μL of 1x PBS +RI. Cells were then counted on a Haemocytometer with Trypan Blue dye and aliquoted into sub-libraries to determine the number of cells to sequence. Approximately 9000 barcoded cells were diluted in 25 μL of PBS +RI and combined with 25 μL of 2x Lysis mix with 5 μL of Proteinase K (Thermo AM2546) for each sublibrary. Lysis was carried out in a thermocyler at 65°C for 1 h and then frozen at −80°C until sequencing library preparation. Complete cell lysis was confirmed by examining lysates under an EVOS FL fluorescent microscope with DiYO dsDNA binding dye (Stratech 17579).

Following cell barcoding, 2 sublibraries of 9000 cells were carried forwards per PDO (x4 total) for cDNA isolation, amplification, and library generation. Sublibrary cDNA isolation and library generation steps were performed at 0.5x volume scale to fit into a thermocycler compatible PCR tube for all temperature incubation steps. Sublibrary cell lysates were thawed at 37°C for 5 min in a thermocycler and neutralized the lysis mixture with 0.45 mM PMSF (Thermo 36978) for 10 min at RT. Biotinylated cDNA was captured and washed with 44 μL of MyOne C1 Dynabeads (Thermo 65001) per sublibrary to as described in.[55] The template switching reaction was performed as described using Maxima H Minus Reverse Transcriptase. Sublibrary cDNA was amplified for 5 (first cycling) + 8 (second cycling) PCR cycles using KAPA HiFi HotStart ReadyMix (Roche KK2601) and subsequently cleaned up using 0.8x SPRI bead size selection with SPRI Kapa Pure Beads (Roche KK8000). Sequencing libraries were generated using the Nextera XT DNA tagmentation (Illumina FC-131-1024), followed by PCR amplification with BC_0118 and one of BC_0076, BC_0077 (PDO21) or BC_0079, BC_0080 (PDO27). Tagmented and amplified sequences were purified with a 0.8x SPRI cleanup and cDNA was quantified (Qubit dsDNA High Sensitivty kit, Thermo Q33230) and the base pair size distribution measured (Agilent High Sensitivity DNA Kit, Agilent 5067-4626). Libraries were then pooled together and loaded onto onto an Illumina Novaseq (200 cycle NovaSeq 6000 S2 Reagent Kit v1.5). The libraries were then sequenced with the following format: R1:74-i7:06-i5:00-R2:86. This sequencing yielded a paired end read structure where the cDNA transcriptomic information was contained in read 1, read 2 was composed of UMI (bp 1–10), BC3 (bp 11–18), BC2 (bp 49–56), BC1 (bp 79–86). Cell barcodes were assigned and reads aligned to the GRCh38 reference genome using the zUMIs package (Version 2.9.7)[52] with STAR version 2.7.3a, filtering on a whitelist of permitted cell barcodes and merging cells that shared the PolyA and Random Hexamer RT1 barcodes from the same RT well plate position with identical L2 and L3 barcodes, counting reads originating from exons and introns. We collapsed cell barcodes with 2 hamming distance of close cell barcodes and UMIs with 1 hamming distance of UMI sequence.

QUANTIFICATION AND STATISTICAL ANALYSIS

TOB*is* mass cytometry data preprocessing

Multiplexed FCS files were debarcoded into separate experimental conditions by using the Zunder Lab Single Cell Debarcoder (https://github.com/zunderlab/single-cell-debarcoder).[19] Debarcoded FCS files were uploaded to Cytobank (Beckman Coulter), gated for Gaussian parameters, and DNA (^{191} Ir/ ^{193} Ir). Epithelial cells were gated on PCK$^+$ and EpCAM$^+$, and CAFs were gated on Vimentin$^+$ and GFP$^+$. Arcsinh transformed values were mean centered across batches before Trellis analysis.

Background in optimal transport for Trellis

Single-cell data are being collected in massively parallel experiments with numerous conditions in order to characterize libraries of treatments[58] including small-molecules[59] and gene-perturbations.[60] One method that directly generalizes bulk measurements to single-cell samples is through the theory of optimal transport and more specifically, the Wasserstein distance.[21–23]

Optimal transport is well suited to the formulation of distances between collections of points, as it generalizes the notion of distances between points to distances between distributions. Intuitively, the distance between distributions should be the minimum total work to move a pile of dirt located at a source distribution to a target distribution. This framework yields a natural definition of similarity between experimental conditions, namely two conditions are similar when their collections of cells are not far from each other.

These distances aim at answering a deeper question: *Which treatments have similar and different effects on the system?* We assume that for each treated condition X we have access to an associated control condition X_c. When all treated conditions are measured relative to a single X_c we show approaches based on the Wasserstein distance are a valid metric between changes in densities. However, in larger experiments it is impossible to measure all treated conditions within a single batch, and thus treated conditions may have different controls. In this case, we show that Wasserstein-based approaches fail, and show that a generalization to an approach based on the *Kantorovich-Rubinstein norm*[61] gives a valid metric between *changes* in densities in this more general multi-control case.

The Wasserstein metric as a norm

Let μ, ν be two probability distributions on a measurable space $\mathcal{X}$ with ground metric $d(x,y)$ between points $(x,y) \in \mathcal{X}^2$, let $\Pi(\mu,\nu)$ be the set of joint probability distributions π on the space $\mathcal{X}^2$ where for any subset $\omega \subset \mathcal{X}$, $\pi(\omega \times \mathcal{X}) = \mu(\omega)$ and $\pi(\mathcal{X} \times \omega) = \nu(\omega)$. The α-Wasserstein distance is defined as:

$$W_d^\alpha(\mu,\nu) = \left(\inf_{\pi \in \Pi(\mu,\nu)} \int_{\mathcal{X}^2} d(x,y)^\alpha \pi(dx,dy) \right)^{1/\alpha}. \quad \text{(Equation 1)}$$

This lifts the ground distance defined between points, to a distance between distributions relative to that ground distance. The *Kantorovich–Rubinstein dual* for the Wasserstein distance on arbitrary measures is

$$\sup_{(f,g) \in C(\mathcal{X})^2} \int_{\mathcal{X}} f(x) d\mu(x) + \int_{\mathcal{X}} g(y) d\nu(y) \quad \text{(Equation 2)}$$

subject to $f(x) + g(y) \leq d(x,y)^\alpha$ for all $(x,y) \in \mathcal{X}^2$. Most work applying the Wasserstein distance focuses on $\alpha = 2$[62] or more general convex costs with $\alpha > 1$,[63] due to the provable regularity of the transport map. We instead focus on the case where $0 < \alpha \leq 1$. Here the transportation map loses regularity but admits a simplification of the dual as when $0 < \alpha \leq 1$, it can be shown that ((2)) achieves optimality when $g = -f$[61] Prop. 6.1 and so simplifies to:

$$W_d^\alpha = \sup_f \left\{ \int_{\mathcal{X}} f(x)(d\mu(x) - d\nu(x)) : \mathcal{H}_d^\alpha(f) \leq 1 \right\} \quad \text{(Equation 3)}$$

where

$$\mathcal{H}_d^\alpha(f) := \sup_{(x,y) \in \mathcal{X}^2} \left\{ \frac{|f(x) - f(y)|}{d(x,y)^\alpha} : x \neq y \right\}. \quad \text{(Equation 4)}$$

When $0 < \alpha \leq 1$, ((3)) shows that W_d^α is the dual of the α-Hölder functions $\{f : \mathcal{H}_\alpha(f) \leq 1\}$ and is a norm, namely

$$W_d^\alpha(\mu,\nu) = \|\mu - \nu\|_{W_d^\alpha}, \quad \text{(Equation 5)}$$

and is valid for any measures μ, ν such that $\int_{\mathcal{X}} \mu = \int_{\mathcal{X}} \nu$. Of particular interest is that W_d^α is still a norm even for non-positive measures. This generalization to non-positive measures will form the basis for our Trellis metric between datasets and is known as the *Kantorovich–Rubinstein norm*[64] when applied to differences of non-positive measures.

Definition 1([64]).

The Kantorovich-Rubinstein (KR) distance between measures μ, ν such that $\int_{\mathcal{X}} \mu = \int_{\mathcal{X}} \nu$ with respect to ground distance d as

$$\mathrm{KR}_d^\alpha(\mu,\nu) := \sup_f \left\{ \int_{\mathcal{X}} f(x)(d\mu(x) - d\nu(x)) : \mathcal{H}_d^\alpha(f) \leq 1 \right\} = \|\mu - \nu\|_{\mathrm{KR}_d^\alpha}. \quad \text{(Equation 6)}$$

For simplicity we will drop the α term and assume $\alpha = 1$, but all statements apply to $0 < \alpha \leq 1$ unless otherwise specified. Trellis can be thought of as an efficient implementation of the KR norm over a tree ground distance.

The Wasserstein distance with tree ground distance

Consider discrete distributions $\mu = \sum_{i=1}^n \mu_i \delta_i$ and $\nu = \sum_{i=1}^n \nu_i \delta_i$ where δ is the dirac function in $\mathbb{R}^d$ and $\sum_{i=1}^n \mu_i - \nu_i = 0$. Then for general costs, the Wasserstein distances between μ and ν can be computed exactly in $\tilde{O}(n^3)$ using the Hungarian algorithm,[65] and approximated using a slightly modified entropy regularized problem in $\tilde{O}(n^2)$ with the Sinkhorn algorithm.[66] However, for some classes of the ground distance, there exist more efficient algorithms (See Table below). For example, if d is the Euclidean distance in $\mathbb{R}$, then the Wasserstein distance can be computed in $O(n \log n)$ time and is equivalent to sorting.[52,67] This special case is exploited in sliced-Wasserstein metrics[68,69] to compute approximate Wasserstein distances in higher dimensions. Another more general class of

ground distances where there exist efficient algorithms is the class of tree metrics. Let $\mathcal{T}$ be a rooted tree with non-negative edge lengths, and let $d_{\mathcal{T}}$ be a *tree metric* on $\mathcal{T}$. Then for two measures μ, ν over $\mathcal{T}$, the Wasserstein distance with respect to $d_{\mathcal{T}}$, $W_{d_{\mathcal{T}}}(\mu, \nu)$, can be computed in $O(n)$ time by exploiting the fact that there is a single path between any pair of masses.[70–72] In this case the 1-Wasserstein distance, also known as the Earth Mover's Distance (EMD) can be expressed as

$$W_{d_{\mathcal{T}}} = \sum_{x \in \mathcal{T}} w_x |\mu(\Gamma(x)) - \nu(\Gamma(x))| \quad \text{(Equation 7)}$$

where w_x is the weight/distance to the parent node of x and $\Gamma(x)$ represents the set of nodes in the subtree of x. Let $P(x, y)$ be the unique path between x and y, then $\Gamma(x) = \{y \in \mathcal{T} | x \in P(r, y)\}$. This alternative formulation can be embedded in l_1:

$$W_{d_{\mathcal{T}}} = \|v(\mu) - v(\nu)\|_1 \quad \text{(Equation 8)}$$

where $v : \mu(\mathcal{T}) \rightarrow \mathbb{R}^n$ is a function such that $v(\mu)_x = w_x \mu(\Gamma(x))$. Approximating the Euclidean distance with a tree distance can be done probabilistically with $O(d \log \Delta)$ distortion in expectation where Δ is a resolution parameter.[73] Following the result of Charikar,[74] this implies that the 1-Wasserstein distance with tree ground distance has the same order distortion. One simple tree construction that achieves this distortion is known as "Quadtree", where each node has four children in $\mathbb{R}^2$ and 2^d children in $\mathbb{R}^d$.[70] We introduce a new tree construction based on *k*-means clustering, which we show is a generalization of the Quadtree construction but can be applied to higher dimensions.

Comparison of Earth Mover's Distance computation methods separated into super-linear (top) and log-linear methods (bottom) based on time-complexity of computing *k*-Wasserstein-nearest-neighbors

Method	Exact	KR-control	Ground cost	*k*-NN-Time
Exact EMD[65]	Yes	No	Any	$O(m^2 n^3)$
Sinkhorn EMD[66]	No	No	Any	$O(m^2 n^2)$
PhEMD[21]	No	No	$d_{\mathcal{M}}$	$O(m^2 T^3 + n^3)$
Mean	No	Yes	Any	$\tilde{O}(kmn)$
Diffusion EMD[22]	No	Yes	$d_{\mathcal{M}}$	$\tilde{O}(kmn)$
Trellis/TreEMD (ours)	Yes	Yes	$d_{\mathcal{T}}$	$\tilde{O}(kmT + n)$

Assumes a dataset of m distributions over n points with (optionally) a tree of size $|T| = O(n)$.

Unpaired and paired Trellis

We start with a more detailed overview of the Trellis algorithm for comparing the effects of drugs on different experimental conditions. The Trellis algorithm is summarized in the below Algorithm. At a high level Trellis consists of four steps.

(1) Construct a tree partitioning of the data T.
(2) Embed each distribution μ^i over $\mathcal{T}$ to a vector $v(\mu^i)$ such that $\text{Trellis}(\mu^i, \mu^j) = \|v(\mu^i) - v(\mu^j)\|_1$ to form a Trellis embedding matrix E.
(3) (optionally) Subtract a control distribution embedding $v(\mu_c^i)$ from each $v(\mu^i)$ for paired Trellis embeddings $\tilde{E}$.
(4) Compute nearest Trellis neighbor distributions exploiting L^1 geometry using fast-nearest-neighbor graph construction algorithms.

$\text{Trellis}(X, \boldsymbol{\mu}, k, l, \mathcal{T}_m, c)$
Input: $n \times f$ data matrix X, $n \times m$ distributions $\boldsymbol{\mu}$, # of clusters k, and # of levels l, manual tree $\mathcal{T}_m$, and (optional) control mapping $\boldsymbol{c}$ specifying control distribution set for each distribution.
Output: $m \times |\mathcal{T}|$ distribution embeddings $\boldsymbol{v}$
$\mathcal{T} \leftarrow \text{BuildTree}(X, k, l, \mathcal{T}_m)$
for Node $\mathcal{T}_i$ with parent edge weight w_i in $\mathcal{T}$ **do**
  $\boldsymbol{v}[:, i] \leftarrow w_i \boldsymbol{\mu}(\Gamma(\mathcal{T}_i))$
end for
if $\boldsymbol{c}$ is *null* **then**
  return $\boldsymbol{v}$
end if
for control distribution set μ_c for each distribution μ in $\boldsymbol{c}$ **do**
  $\boldsymbol{v}[\mu] \leftarrow \boldsymbol{v}[\mu] - \text{mean}_{\mu_c}(\boldsymbol{v}[\mu_c])$
end for
return $\boldsymbol{v}$

We next discuss potential methods of constructing $\mathcal{T}$, how to embed an empirical distribution to a vector and its equivalence to the Wasserstein distance, the effect of subtracting a control distribution embedding, and finally how to construct a Trellis-metric nearest neighbor graph for subsequent visualization with a non-linear embedding algorithm such as PHATE,[50] UMAP,[75] or *t*-SNE.[76]

Constructing trees on single-cell mass cytometry data

Trellis gives a distance between measures or differences in measures over a tree metric space. Often the data is not associated with an explicit tree metric, but is naturally hierarchical such as in the case of single-cell cytometry data. Previous methods have used manual gating, automatic gating, or a combination of the two to hierarchically cluster single-cell mass cytometry data.[77] These methods build trees, but are missing the 'metric' component, which can be encoded as the edge weights between parent and child clusters. We use a simple tree metric where each edge weight for node x is the Euclidean distance between the cluster center $\text{mean}(x)$ and the center of its parent $\text{mean}(Pa(x))$.

$$w_x = \| \text{mean}(x) - \text{mean}(Pa(x)) \|_2. \quad \text{(Equation 9)}$$

The tree metric between two nodes $u, v \in \mathcal{T}$ is the sum of the path lengths along the unique path geodesic between u and v in $\mathcal{T}$ denoted by $P_{\mathcal{T}}(u, v)$ then

$$d_{\mathcal{T}}(x, x) = \sum_{v \in P_{\mathcal{T}}(x,y)} w_v. \quad \text{(Equation 10)}$$

Trellis applies to any clustering method; we demonstrate the Trellis framework using a simple combination of manual gating for non-Euclidean features and automatic gating to approximate Euclidean distances among sub populations. This strategy allows us to leverage manual gating when appropriate and follows the experimental design, or automatic gating using repeated unsupervised *k*-means clustering on the biological splits. This clustering method is of particular interest because in specific settings we can show that the Trellis metric is topologically equivalent to an Wasserstein distance with Euclidean ground distance in $\mathbb{R}^d$. Given a number of clusters at each level k and a depth h construct a divisive tree-like clustering of the data as described in the below Algorithm. Where Kmeans is the *k*-means algorithm with some fixed set of parameters. Interestingly, with a specific setting of *k*-means we show Trellis is topologically equivalent to the α-Wasserstein distance with Euclidean ground distance. This is formalized in the following proposition.

BuildTree$(X, k, l, \mathcal{T}_m)$
Input: $n \times f$ data matrix X, # of clusters k, # of levels l and (optional) manual base tree $\mathcal{T}_m$.
Output: Weighted clustering tree $\mathcal{T}$.
if $l = 0$ **then**
  return *null*
end if
if $\mathcal{T}_m$ is not *null* **then**
  for leaf node n_i in $\mathcal{T}_m$ **do**
    $\mathcal{T}_i \leftarrow$ BuildTree$(X[n], k, l, null)$
  end for
  //Where TreeJoin replaces each of the leaves with the respective subtree
  return $\mathcal{T} \leftarrow$ TreeJoin$(\mathcal{T}_m, [\mathcal{T}_i])$
end if
labels $\leftarrow$ Kmeans(X)
for $i = 1$ to k **do**
  $\mathcal{T}_i \leftarrow$ BuildTree$(X[labels = i], k, l - 1)$
end for
return $\mathcal{T} \leftarrow [\mathcal{T}_i]_{i=1}^{k}$

Proposition 1

Let $k = 2^d$, $max\_iter = 0$, data X be normalized such that $X \in [-1, 1]^d$ with precision Δ and initialize the k^{th} cluster at level l with parent center p as $p + 2^{1-l}(Binary(k) - 1/2)$. Then there exists constants c, C such that

$$c \cdot W_{\|\cdot\|_2}(\mu, \nu) \leq \mathbb{E}[\text{Trellis}(\mu, \nu)] \leq C \log\Delta \cdot W_{\|\cdot\|_2}(\mu, \nu). \quad \text{(Equation 11)}$$

This can be seen by first noting that this initialization is equivalent to a QuadTree construction in the topological sense. If two points are clustered together in our construction at some level then they are also clustered together in QuadTree at the equivalent level. In addition, the edge weights are equivalent up to a constant with the edge weights decaying by $1/2$ at every level in both constructions. Once these two properties are verified, then we can leverage existing results on QuadTree constructions from[70] and[74] to show that the inequalities hold. We also note that there exist results on the approximate nearest neighbors of this construction in.[72] While this relates tree distances using *k*-means clustering to the Euclidean ground distance, interestingly, this proposition can be applied more generally to any

embedding space allowing us to link tree distances to general ground metrics defined over embeddings. For example, *k*-means is often also applied in a Laplacian embedding space, which is known as *spectral clustering*.[78] Here it is easy to show that the *k*-means based tree construction in Proposition 1 relates the Trellis distance to the Wasserstein distance with spectral ground distance distance. While these parameters for *k*-means-clustering work well in low dimensions, the number of clusters scales exponentially with dimension. In practice we use four levels of four clusters. This expectation holds over a randomly selected initialization of the zero'th level cluster. In practice, we take the expectation over *k*-means initializations, building ten parallel trees with different initializations. Trellis can be applied to any tree metric or ensemble of tree metrics. We have presented a method that allows for combining manual and automatic gating, as well as an automatic gating method that in expectation is similar to a Euclidean distance. Many other choices for partitioning CyTof data have been explored in the automatic gating literature.[77,79–81] These automatic gating methods are generally used for partitioning the data not building a tree metric. However, it is simple to convert them into tree metrics by assigning edge weights based on cluster means. This strategy can be applied to a precomputed tree-like clustering of the data with no knowledge of how those clusters were chosen. This allows for adaptation of Trellis to different systems where either manual or automatic gating is preferred or already computed.

Trellis given a metric tree

Given a general metric tree $\mathcal{T}$ of size $|\mathcal{T}|$, we first define the embedding function $v : \mu(\mathcal{T}) \rightarrow \mathbb{R}^{|\mathcal{T}|}$ which takes distributions defined over the tree and embeds them in a vector space where the L^1 between vectors is equivalent to the Wasserstein distance with tree ground distance. Given edge weights w_x and denoting the subtree at node x as $\Gamma(x) = \{y \in \mathcal{T} | x \in P(r,y)\}$, then v is defined element-wise as

$$v(\mu) = [w_x \mu(\Gamma(x))]_{x \in \mathcal{T}}. \quad \text{(Equation 12)}$$

Intuitively, this can be thought of computing the sum of the mass below each node times the edge weight at each node. The difference between $v(\mu)_x - v(\nu)_x$ for a given node $x \in \mathcal{T}$ can be thought of as the amount of work needed to move μ to ν. If this difference is positive, then this means that mass of μ is greater in the subtree $\Gamma(x)$ than the mass of ν. This means that the transport map must move exactly $\mu(\Gamma(x)) - \nu(\Gamma(x))$ mass upwards from x at cost w_x. Adding up these aggregate movements over all nodes gives the total work needed and is equivalent to the work required by the Wasserstein distance. For our tree construction with the additional manual tree step, we define the unpaired Trellis distance (uTrellis) as

$$\text{uTrellis}(\mu, \nu) = \|v(\mu) - v(\nu)\|_1. \quad \text{(Equation 13)}$$

We also define a Tree-Earth Mover's Distance (TreEMD) without the manual tree construction, considering only the *k*-means construction. TreEMD is similar to previous Tree-based Wasserstein distance constructions for high dimensions.[71,72] These two unpaired distances are comparable to existing methods for computing the Wasserstein distance between distributions. However, these distances do not take into account control, treatment, batch, and replicate information. Given information on which samples were taken under similar conditions, we are able to improve the distances with *Paired Trellis*.

Paired Trellis

To examine the effects of a drug across many conditions it is useful to measure the differences of the treated condition relative to a matched control. For each sample μ and ν, let the associated control distributions be μ_c and ν_c respectively, and v be defined as above. Then we define the Paired Trellis metric between changes in distributions as:

$$\text{pTrellis}(\mu, \nu) := \|v(\mu) - v(\mu_c) - v(\nu) - v(\nu_c)\|_1.$$

Intuitively, the Paired Trellis distance measures the difference in the change in density between treated conditions from their respective controls. This allows us to control for unmeasured confounders that are implicit in the treated cell population μ and ν respectively.

Proposition 2

For two distributions μ, ν with their respective controls μ_c, ν_c, the Paired Trellis is equivalent to a Kantorovich-Rubenstein distance with tree ground distance as in ((7))

$$pTrellis(\mu, \nu) = KR_{d_\mathcal{T}}(\mu - \mu_c, \nu - \nu_c). \quad \text{(Equation 14)}$$

Proof. The equivalence of paired Trellis to a Kantorovich-Rubenstein distance can be verified through algebraic manipulation following.[82] We start with the definition of the Kantorovich-Rubenstein distance and show that this is equivalent to pTrellis for an arbitrary tree domain $\mathcal{T}$ with ground distance $d_\mathcal{T}$. Denote the family of Hölder functions under $d_\mathcal{T}$ as $\mathcal{F} = \{f : \mathcal{H}^\alpha_{d_\mathcal{T}}(f) \leq 1 \,\&\, f(r) = 0\}$ and let λ be the (unique) length measure on $\mathcal{T}$ such that $d_\mathcal{T}(x,y) = \lambda(P(x,y))$. Then there exists a unique function $g: \mathcal{T} \rightarrow [-1, 1]$ such that $f(x) = \int_{P(r,x)} g(z)\lambda(dz) = \int_\mathcal{T} 1_{z \in P(r,x)} g(z)\lambda(dz)$.

$$\int_\mathcal{T} f(x) d\mu(x) = \int_\mathcal{T} \int_\mathcal{T} 1_{z \in P(r,x)} g(z)\lambda(dz) d\mu(x) = \int_\mathcal{T} g(z)\mu(\Gamma(z))\lambda(dz). \quad \text{(Equation 15)}$$

For the optimal witness function f^*, we have

$$g(z) = \begin{cases} 1 & \text{if} \mu(\Gamma(z)) > \nu(\Gamma(z)) \\ -1 & \text{else} \end{cases}. \quad \text{(Equation 16)}$$

Plugging this equivalence into Equation 6 we have

$$KR_{d_\mathcal{T}}(\mu,\nu) = \sup_f \left\{ \int_\mathcal{T} f(x)(d\mu(x) - d\nu(x)) : \mathcal{H}^\alpha_{d_\mathcal{T}}(f) \leq 1 \right\} = \int_\mathcal{T} |\mu(\Gamma(z)) - \nu(\Gamma(z))| \lambda(dz). \quad \text{(Equation 17)}$$

Therefore, for two measures a, b over $\mathcal{T}$ such that $\int_\mathcal{T} a(x)dx = \int_\mathcal{T} b(x)dx = c$ we have that $a(\Gamma(r)) = b(\Gamma(r)) = c$ and for $v: \mathcal{T} \to \mathbb{R}^+$ as defined in Equation 12 we have

$$KR_{d_\mathcal{T}}(a,b) = \sum_{x \in \mathcal{T}} w_x |a(\Gamma(x)) - b(\Gamma(x))| = \|v(a) - v(b)\|_1. \quad \text{(Equation 18)}$$

substituting $a = \mu - \mu_c$ and $b = \nu - \nu_c$ yields the proposition since $\int_\mathcal{T} a = \int_\mathcal{T} b = 0$ for any distributions $\mu, \mu_c, \nu,$ and ν_c.

We ablate both the pairing and manual tree construction steps in Figure S1. A paired Trellis embedding better separates the effects of increased drug concentration as compared to TreEMD (Figure S1C) and an unpaired Trellis embedding according to a k-NN classifier trained with 10-fold cross validation, while also being less sensitive to batch effects by the same metric (Figure S1B).

Nearest Trellis neighbors

Fast nearest neighbor calculation is useful in graph-based methods which use the k-nearest neighbor graph for down stream tasks such as clustering,[78] classification,[72] or visualization.[50,75,83] In this paper, for example we visualize the space of all experimental conditions using PHATE[50] (Figures 3, 4, 5, and 6). For nearest neighbors in normed spaces such as the L^2 norm, the geometry of the space can be utilized for fast exact or approximate nearest neighbor calculation in time scaling logarithmically with the number of points. For more general distances between objects, these algorithms may not apply. For instance, to compute the k-nearest neighbor distributions in terms of the Wasserstein distance for m distributions, there is no faster algorithm than computing the Wasserstein distance to all other distributions then computing the k closest ones in $O(m)$ time. However, the Unpaired and Paired Trellis versions of the Wasserstein distance for finite data can be expressed as norms in a finite dimensional space, this allows us to apply fast nearest neighbor algorithms which exploit the induced geometry between distributions. In this case, to find nearest neighbor distributions we can apply tree-based algorithms such as KD-Trees, or Ball-Trees as used in PHATE[50] and scikit-learn,[84] locality sensitive hashing in $O(T \log m)$ time for m distributions on trees of size T.

Visualizing Trellis embeddings

Trellis embeds measures μ in a metric space endowed with a Tree-Wasserstein distance to vectors v in $\mathbb{R}^{|\mathcal{T}|}$ with the L^1 metric. These embeddings can be further embedded into $\mathbb{R}^2$ using a non-linear dimensionality reduction which relies on fast k-nearest-neighbors calculations. We make extensive use of Trellis-PHATE, which further embeds Trellis (or paired Trellis) embeddings into 2D for visualization and exploratory analysis. Trellis-PHATE takes the embedding matrix $\boldsymbol{E}$ or $\tilde{\boldsymbol{E}} \in \mathbb{R}^{m \times |\mathcal{T}|}$ as a data for the PHATE algorithm with the additional argument KNN_DIST = "manhattan" to encode the L^1 metric between Trellis embedding vectors. The PHATE algorithm then gives a PHATE embedding $\boldsymbol{E}^{PHATE} \in \mathbb{R}^{m \times 2}$ which can be visualized as a scatterplot of m points (one per sample) in 2D as shown in Figures 3, 4, 5, S1, S2, S4, and S5. We note any other dimensionality reduction method could be chosen that can take vectors embedded in an L^1 vector space as input such as t-SNE[76] or UMAP.[75]

Parameter robustness

Trellis has a few important parameters that may affect the resultant output. In Figure S2C, we test the effect of these parameters on the Trellis distances on the PDO dataset. Specifically, we compare the effects of changing the default number of trees $|\mathcal{T}|$, the depth of the automatic tree construction l, and the number of clusters used at each level c. We default to 10 trees with 4 levels of 4 clusters. We measure how much the Trellis distances between samples change relative to this default setting. We test $|\mathcal{T}| \in \{1, 5, 10, 50\}$, $l \in \{2, 3, 4, 5, 6\}$, and $c \in \{2, 3, 4, 5, 6\}$. We ablate each parameter individually and measure the correlation in distance matrices between samples with the Spearman R correlation, and the precision of the 50 nearest neighbors. The Spearman correlation measures the overall correspondence between distances and remains extremely high at >0.9 for all settings (and >0.98 for all neighboring settings). Since we are interested in constructing manifolds of samples using non-linear dimensionality reduction, we are particularly interested in the nearest-neighbor samples, which affect the graph construction. Here the P@50 metric measures for each sample how many of the 50-nearest-neighboring samples in the reference setting are in the set of 50-nearest-neighbors of the test setting. This can be summarized in the following equation:

$$\text{P@k}(\boldsymbol{D}^{test}, \boldsymbol{D}^{ref}) = \frac{1}{n} \sum_{i=1}^{n} \frac{\left| \text{k\_argmin}(\boldsymbol{D}_i^{test}) \cap \text{k\_argmin}(\boldsymbol{D}_i^{ref}) \right|}{k}$$

where we use $k = 50$, i indexes into the samples of the distance matrices $\boldsymbol{D}$, and the k-argmin returns the set of k indices with the smallest values. We see a majority (>0.5) of the nearest neighbors are preserved in all settings. This is quite high given the classification over >3,000 individual samples, where a random sampling would give $P@50$ of <0.02.

Related work and time complexity

There are many methods for computing or approximating the Wasserstein distance. In Table we present methods for computing the nearest neighbor distributions according to the Wasserstein distance split into two groups. Here we consider the time it takes for the method to compute the k-Wasserstein-nearest-neighbors on a dataset with m distributions over n points with access to a precomputed tree over the data of size $|T| = O(n)$. The first three methods are widely used, but do not scale well to large datasets with a large number of distributions or a large number of points. For the first three methods, the Hungarian algorithm,[65] the Sinkhorn algorithm,[66] and Phenotypic Earth Mover's Distance (PhEMD),[21] to find the k-nearest-neighbors for a distribution it is necessary to compute the distance to all m other distributions. This implies that they scale poorly with the number of distributions as illustrated in S2b. PhEMD saves significant time by only computing the distances between a small set of clusters, however, eventually this is dominated by an increasing number of distributions. Trellis and TreEMD scale log linearly in the number of points, distributions, and the size of the precomputed tree $\mathcal{T}$. Constructing the tree partitioning for Trellis takes $\tilde{O}(n)$ time. Embedding the distributions takes $O(mT)$ time. Subtracting the control distribution embedding for paired Trellis takes $O(T)$ time. finally, computing the k-nearest neighbors of the Trellis distance takes $\tilde{O}(kmT)$ time. In total both unpaired and paired Trellis take $\tilde{O}(kmT + n)$ time to compute the k nearest neighbor distributions. When $T \ll n$ as in our case, we can see substantial increases in speed in line with simply taking the Euclidean distance between means of clusters. As T achieves its upper bound of $2n - 1$, Trellis has the same complexity as computing the nearest distribution means and of DiffusionEMD.[22]

Single-cell RNA-seq data pre-processing and quality control

Each sublibrary's digital gene expression matrix (DGE) was processed with the splitRtools package (https://github.com/TAPE-Lab/splitRtools) to annotate each cell barcode with sample-specific and well-specific barcoding SPLiT-seq information. Downstream analysis was performed in Scanpy.[51] Sublibrary DGEs were then merged per PDO and trimmed to exclude low quality cells based on the following parameters, <1000 UMIs, <20% mictochondrial transcripts, <400 genes detected and outliers with high numbers of genes that were >(median(log10(UMI)) + 2*IQR) and likely represented cell doublets. Genes that were not detected in at least 25 cells were further removed. We used scrublet[85] to remove neotypic doublets on a per PDO basis with an expected doublet rate of 3% (n = 244 cells), before merging both PDO datasets. Cells were then normalized by a size factor of 10000 excluding highly expressed genes for the computation of the size factor if it has more than 5% of the total counts in at least one cell. The normalised data was then natural log transformed for downstream analysis. An initial exploration of the data was performed using a coarse SNN-based clustering, scaling the data and performing PCA over 5000 variable genes and building an SNN graph (n_pcs = 50, n_neighbbors = 100) and clustered the cells using the leiden implementation (res = 0.1) to identify either PDO or Fibroblast and removed barcoding collisions for monoculture samples that clustered an alternate cell type (n = 26 cells). This workflow yielded a dataset of high-quality single cells (n = 31572, median UMI = 2552, median genes = 1282) with a low overall mitochondrial fraction of transcripts (median = 0.07). Using this trimmed dataset the clustering procedure was repeated to generate a final cell type assignment.

Single-cell RNA-seq perturbation analysis with MELD

In order to leverage the ability to multiplex multiple replicate samples using SPLiT-seq, MELD was used to identify PDO cellular populations for each PDO sample that are enriched or depleted based on co-culture with CAFs.[30] MELD is a manifold-geometry based method of quantifying the effect of an experimental perturbation by estimating the relative likelihood of observing cells in each experimental condition over a graph learned from all cells in a sample. PHATE embeddings of all cells per PDO were used for visualisation purposes only of the scRNA-seq data. However, if all conditions and replicates were analyzed all together certain samples might be over-represented in a given manifold and we therefore may lose important enrichment information. To preserve enrichment information across replicates one density estimate was generated per experimental replicate and then L^1 normalization was applied to these densities within each replicate to normalize the values to sum to 1 across samples within each replicate. We used the average likelihood of the PDO co-culture samples as the measure of perturbation.

Generation of single-cell RNA-seq expression signature scores

All gene expression signature scores were computed as previously described in[86] by defining an input set of literature curated signature genes (Table S5) and comparing their average relative expression to that of a sampled control gene set.[29,32,35,87–90] The control gene set was randomly sampled to mirror the expression distribution of the genes used for each binned expression value. proCSC and revCSC gene signatures were derived from curated literature sources describing these transcription programs and where genes signatures were derived from murine systems, gene homologs were identified with biomart.[91] Gene signatures were further filtered to keep genes that were detected in at least 320 PDO 21 cells or 50 PDO 21 cells for the enteroendocrine signature before computing the signature score. Gene expression signature score trends over MELD score for each replicate were computed using a linear

generalized additive model (GAM) of 10 cubic splines using the python package pyGAM.[92] The average GAM model value of the three replicates was used for visualization along with the upper and lower 95% confidence interval.

Single-cell RNA-seq VR landscapes

Valley-Ridge (VR) scores were computed as described in Qin & Cardoso Rodriguez et al.[29] The VR score is a cellular metric computed on a per sample (mono-culture or co-culture) and cluster (defined with Leiden clustering at res = 0.2) labels and is defined as the weighted sum of the two components: CCAT signalling-entropy[93] and RNA velocity vector length.[94] CCAT has been defined as an estimate for a cell's Signaling Entropy Rate, which has been shown to be a robust metric for cellular pluripotency.[93,95,96] RNA velocity vector lengths are the modulus of the inferred RNA velocity vectors as determined by a cell's ratio of spliced and unspliced mRNA, thus measuring the overall rate of transcriptomic change undergone by a cell. In brief, the CCAT scores and RNA velocity vector lengths were computed on all epithelial cells from the PDO21 mono- and co-culture conditions. At a cluster's center, the VR score is solely determined by the median CCAT. However, the VR scores at the cluster periphery are augmented by weighting the inverse of scaled RNA velocity component and the scaled distance from the cluster center. We use the inverse of the velocity vector length to model rates of local transcriptional change, so that transitions substantiated by high RNA velocities do not locally increase landscape elevation at a cluster's boundary, with the opposite happening for low velocity cells. To generate the landscapes in Figure 7 we projected the VR scores into the PHATE embedding of PDO21 cells (Figure 6A) using the 3D rendering software SideFX Houdini and Maxon Redshift. After the VR scores were used to interpolate the landscape surface, individual cells were overlaid on the surface and colored according to their relative expression of *MKI67*. A full step-by-step protocol for generating VR landscapes can be found in Qin & Cardoso Rodriguez et al.[29]

CellPress
OPEN ACCESS

Supplemental figures

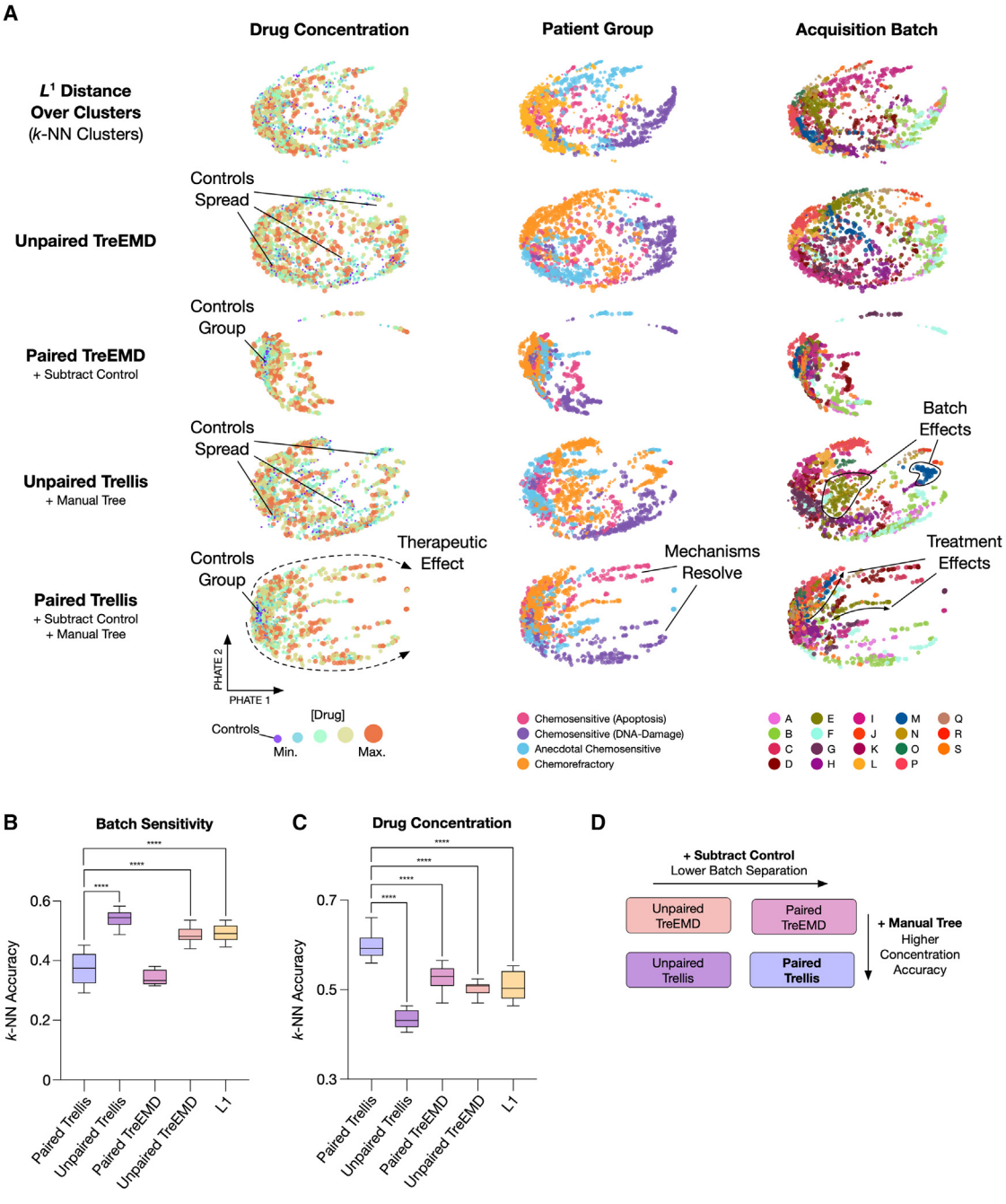

Figure S1. Trellis ablation test, related to Figure 2

(A) Comparison of Trellis' ablated algorithm into L^1 distance over *k*-NN clusters, Wasserstein distance over automatic gating (Unpaired TreEMD), Kantorovich-Rubenstein (KR) norm over automatic gating (Paired TreEMD), Wasserstein distance over tree partitions of the data by cell state (Unpaired Trellis), and KR norm tree partitions of the data by cell state (Paired Trellis).

(B) *k*-NN accuracy score on acquisition batches. A higher *k*-NN accuracy infers a higher batch separation effect by the method.

(C) *k*-NN accuracy score on drug concentrations vs. controls. Paired Trellis improves drug treatment effect detection.

(D) Schematic representation of the comparison across methods. One-way ANOVA, **** < 0.0001 (n = 10).

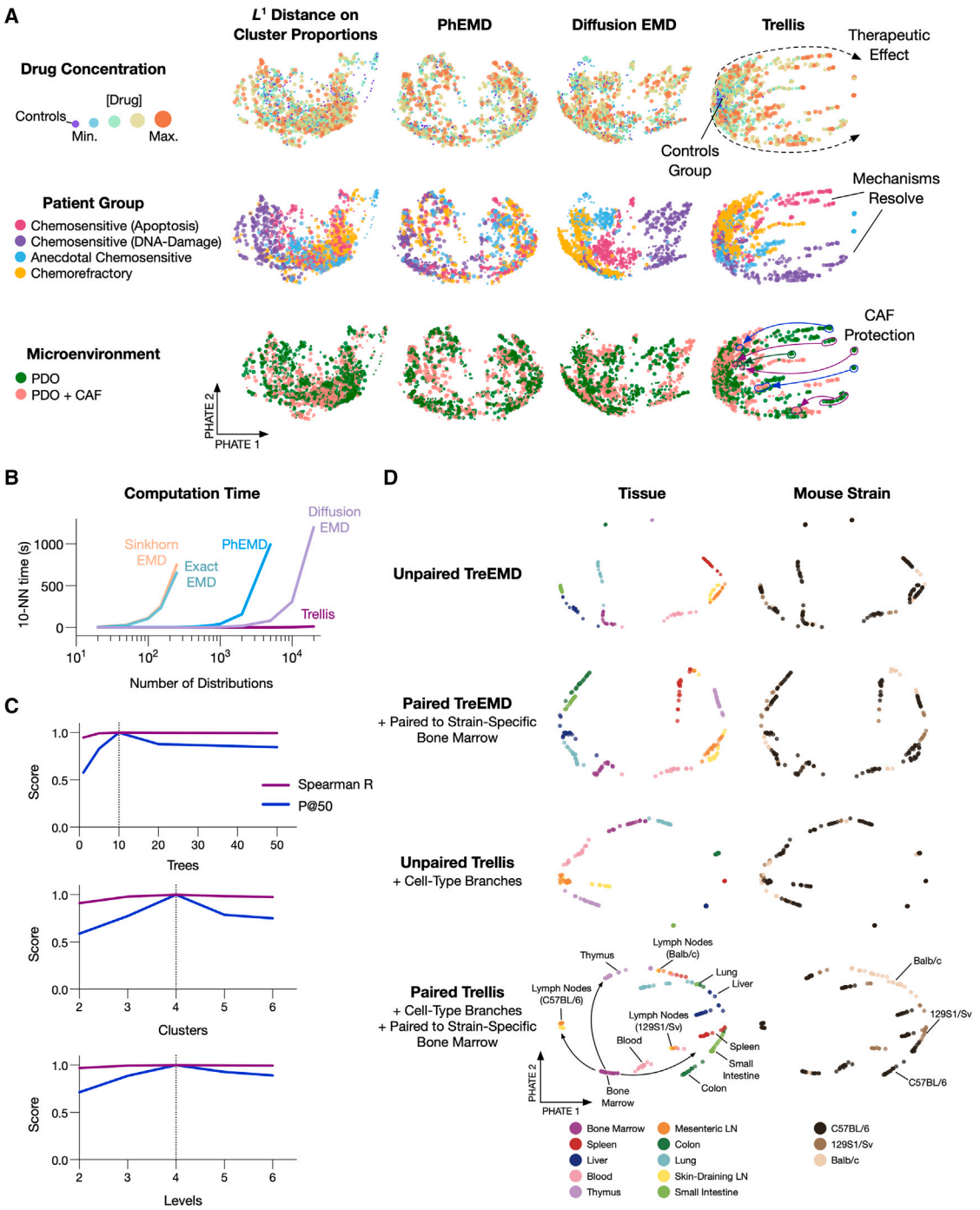

Figure S2. Comparison of Trellis to alternative methods and datasets, related to Figure 2

(A) Trellis performance compared to existing methods such as L^1 distance of differential abundance of cells in clusters, PhEMD, and Diffusion EMD. Alternative methods fail to capture therapeutic effects and cannot identify CAF protection.

(B) Trellis speed and scalability relative to alternative EMD methods.

(C) Analysis of Trellis sensitivity to its three components—number of trees, clusters, and levels—demonstrates a strong stability when manipulating these components.

(D) Trellis analysis of murine immune cell atlas. Unpaired TreEMD, Paired TreEMD (paired to bone marrow control), Unpaired Trellis (using immune cell-type branches), and Paired Trellis (using immune cell-type branches, paired to bone marrow control) analysis of murine immune atlas mass cytometry data (from Spitzer et al.[97]; 202 single-cell datasets). All tree-based methods resolve tissue-specific immune profiles, but Paired Trellis also captures broad hematopoietic development trajectories and reveals mouse-strain-specific differences (specifically regarding strain-specific lymph node profiles).

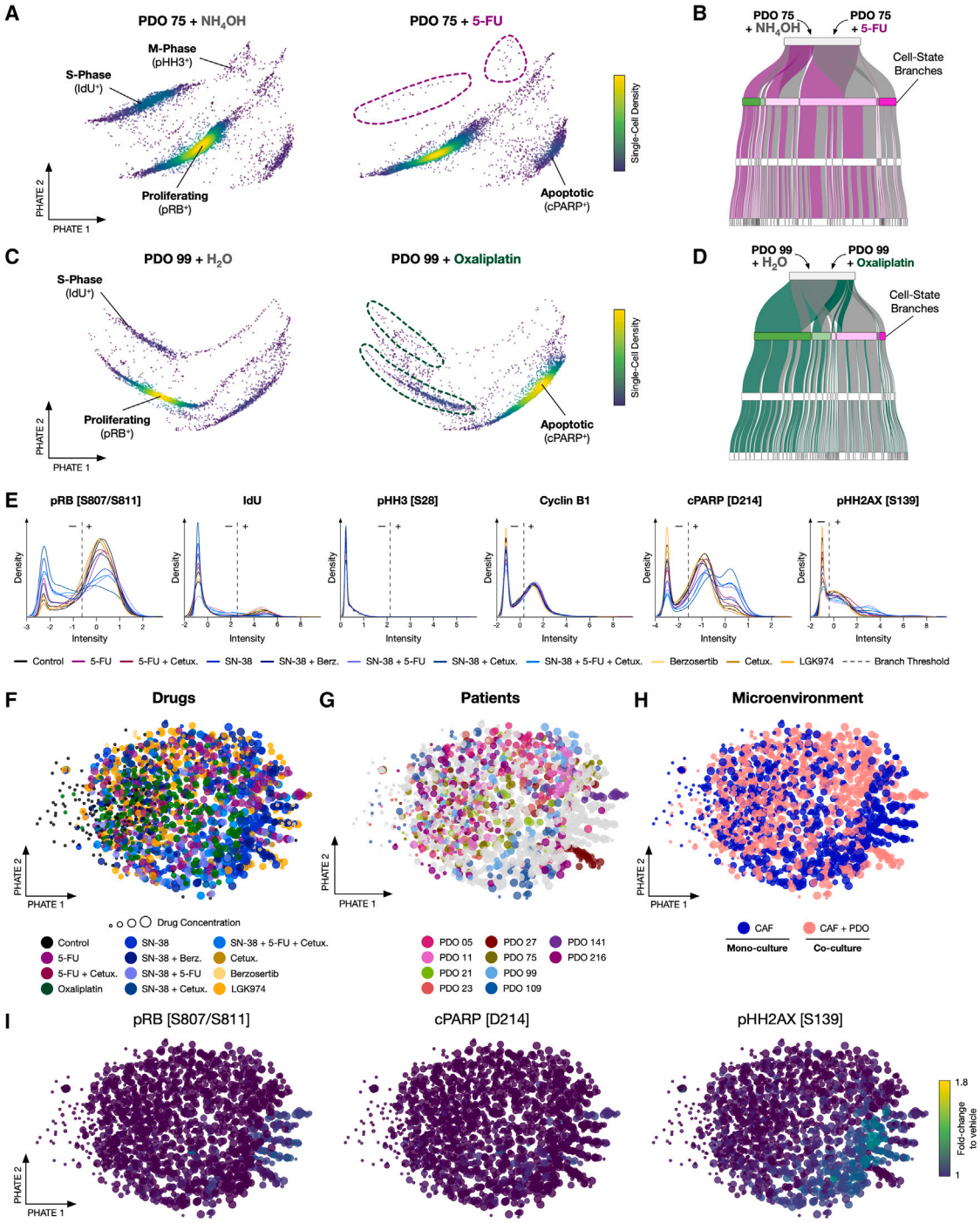

Figure S3. Trellis detection of PDO and CAF cell-state drug responses, related to Figures 2 and 3

(A) Single-cell density PHATEs of PDO 75 treated with NH_4OH vehicle control or 5-FU.

(B) Sankey diagram showing data from (A) distributing through the cell-state Trellis layout in Figure 2 (terminal leaves not shown).

(C) PDO 99 treated with H_2O vehicle control or Oxaliplatin.

(D) Sankey diagram showing data from (C) distributing through the cell-state Trellis layout in Figure 2 (terminal leaves not shown).

(E) Trellis cell-state branch thresholds for PDO 21 (batch-mean centered and arcsinh transformed intensities). Thresholds are designed based on prior knowledge and adjusted manually following classical cytometry gating by setting the limit of a population on the edges.

(F–H) Trellis-PHATE of PTM profiles from PDO-CAF cultures fails to identify (F) drug-specific CAF responses, (G) patient-specific CAF drug responses, or (H) microenvironment-specific CAF drug responses.

(I) Fold-changes to vehicles of pRB [S807/S811], cPARP [D214], and pHH2AX [S139] fail to resolve drug- or patient-specific shifts in cell state.

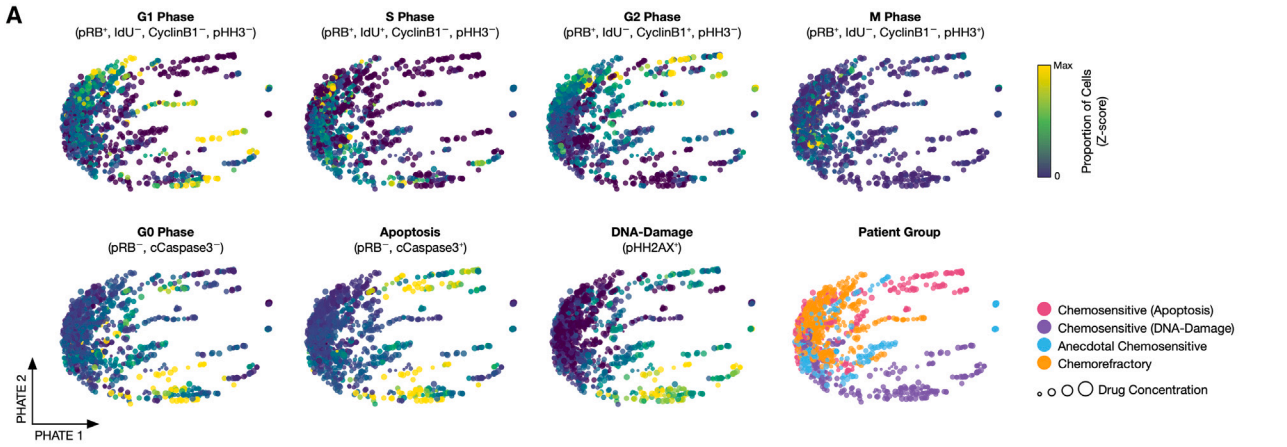

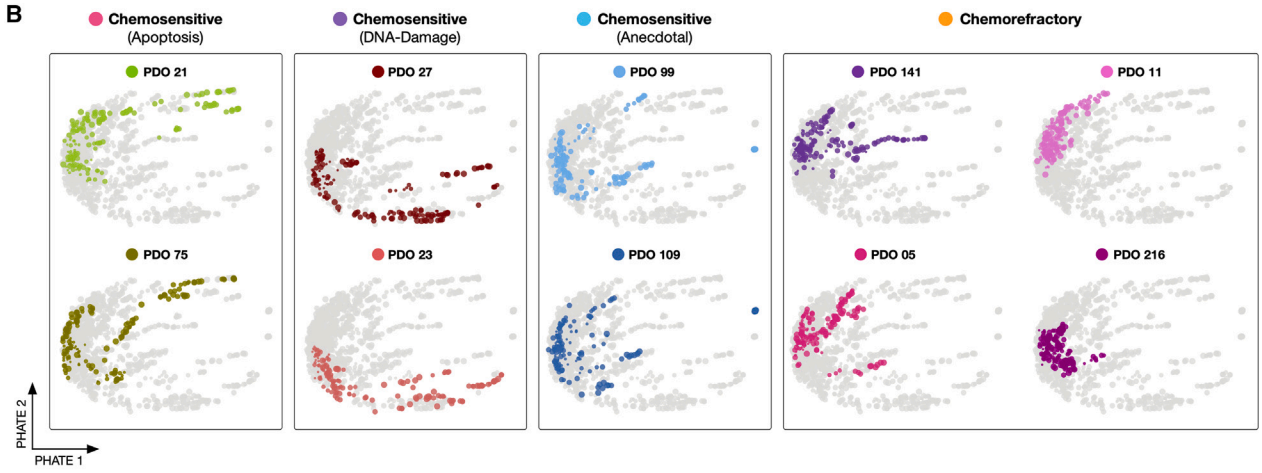

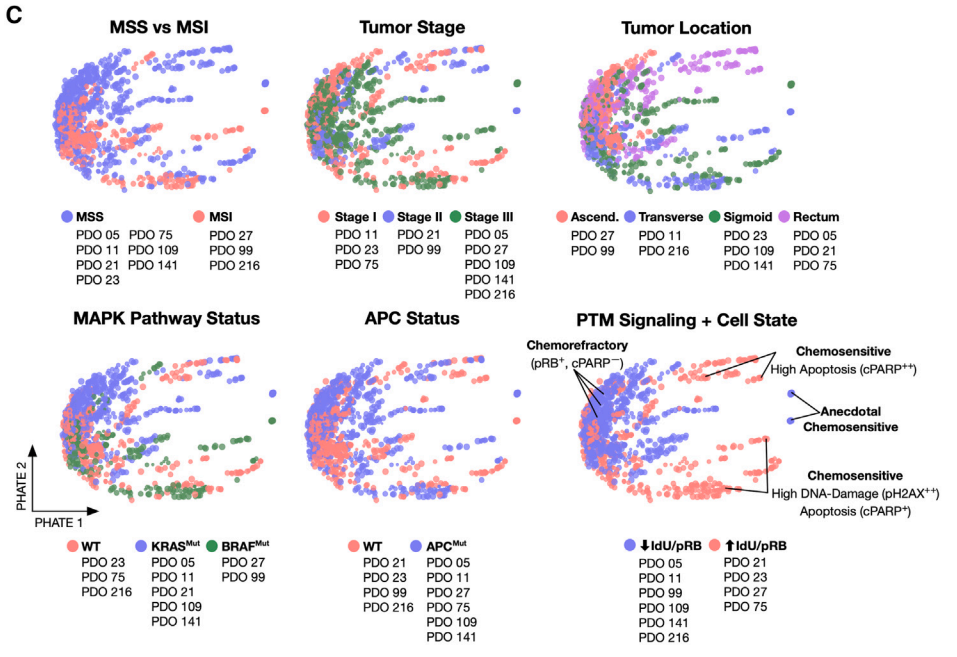

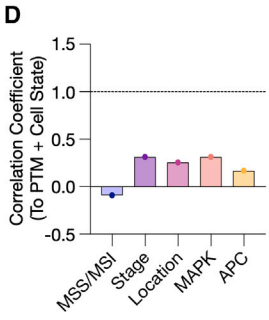

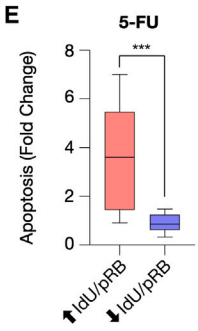

(legend on next page)

Figure S4. PDO Trellis-PHATE cell-state distributions, related to Figures 3 and 4

(A) Cell-state proportions (*Z* score) across 1,680 single-cell PDO cultures reveal PDO-specific mechanistic drug treatment effects.

(B) Individual patient distributions on Trellis-PHATE embedding show patient-specific mechanisms of response: chemosensitive PDOs spread across the PHATE 1, activating mechanisms of DNA damage and/or apoptosis, while chemorefractory PDOs show similar positions on the Trellis-PHATE embedding to their internal controls, suggesting minimal responses to treatments.

(C) Trellis-PHATE plots of patient metadata. Patient-specific treatment effects do not align with MSS/MSI, tumor stage, tumor location, MAPK pathway mutations, or APC mutations. High baseline cell-cycle activity correlates with broad chemosensitivity.

(D) Quantification of the correlation between PDO metadata information and PDO cell state. Unpaired *t* test, *** < 0.0001.

(E) Quantification of 5-FU chemocytotoxicity in low- and high-cycling PDOs.

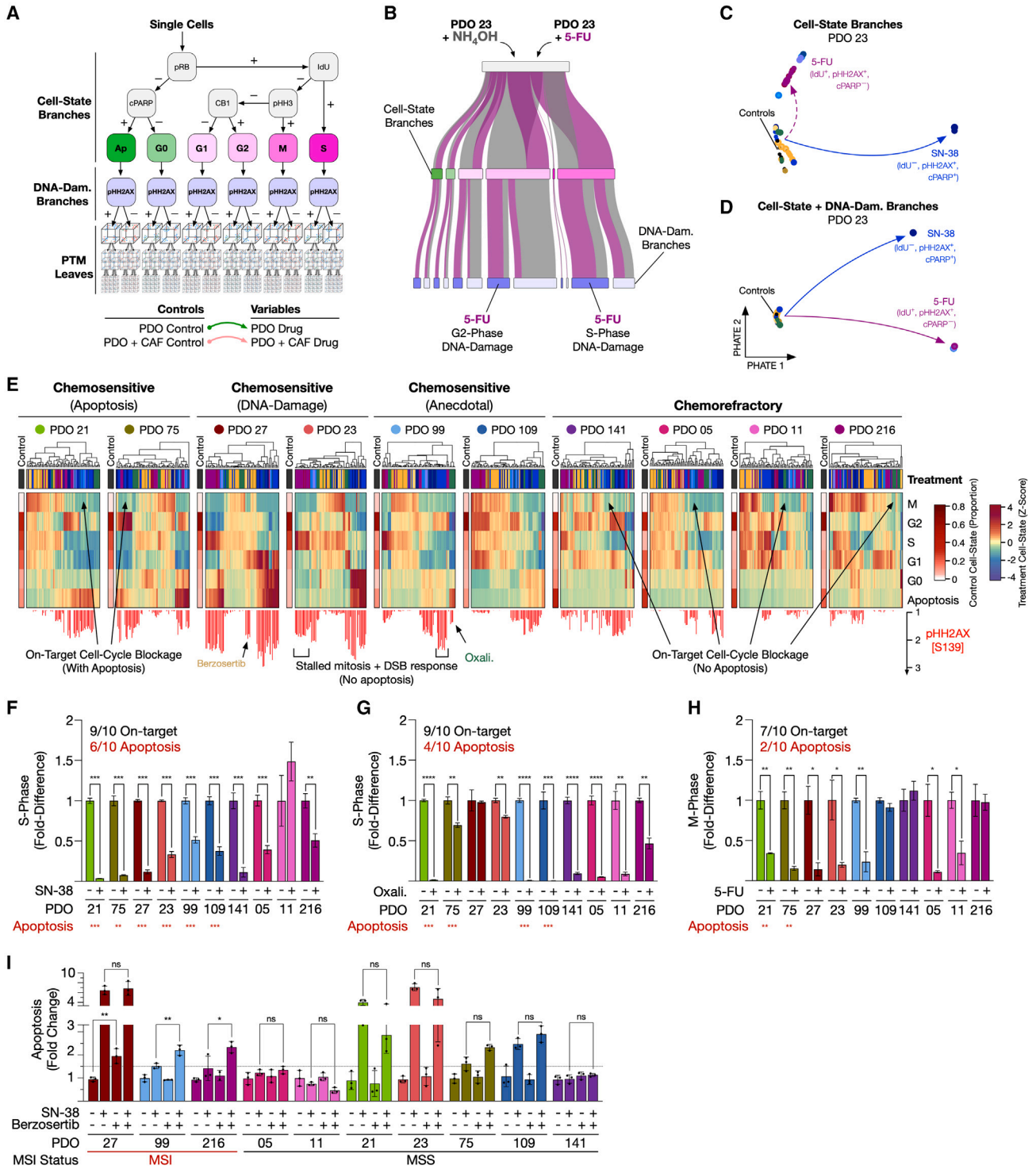

Figure S5. Patient-specific regulation of cell state and DNA damage, related to Figure 4

(A) Trellis tree containing cell-state branches with a pHH2AX [S139] DNA double-strand break detection layer.

(B) Sankey diagram showing NH_4OH vehicle control and 5-FU treatment of PDO 23 distributing through the cell-state and DNA-damage-driven Trellis branches in (A) (leaves not shown).

(C and D) Trellis-PHATE of PDO 23 treatments analyzed using (C) cell-state branches alone or (D) cell-state branches and pHH2AX [S139] detection layer. The DNA-damage detection layer improves resolution of 5-FU on-target treatment effect. Solid arrows refer to strong treatment effect; dashed arrows refer to partial treatment effect.

(legend continued on next page)

(E) Patient-specific distribution of cells within Trellis branches reveals mechanistic cell-state shifts and DNA damage upon drug treatments. Treatment cell state quantifies the fold change of the proportion of cells/cell state over the controls for each treatment (*Z* score). DNA damage is quantified by the fold change of the proportion pHH2AX^{+} cells over the controls.
(F) PDO cells in S-phase following 100 nM SN-38.
(G) PDO cells in S-phase following 200 nM Oxaliplatin.
(H) PDO cells in M-phase following 200 nM 5-FU. PDOs with a significant >1.5-fold increase in apoptosis are indicated in red.
(I) PDO apoptosis following treatment with SN-38 and/or Berzosertib. Only MSI PDOs are sensitive to ATR inhibitors either alone (PDO 27) or in combination with SN-38 (PDOs 99 and 216). Unpaired *t* test using three replicates, *** < 0.0001, ** < 0.001, * < 0.01.

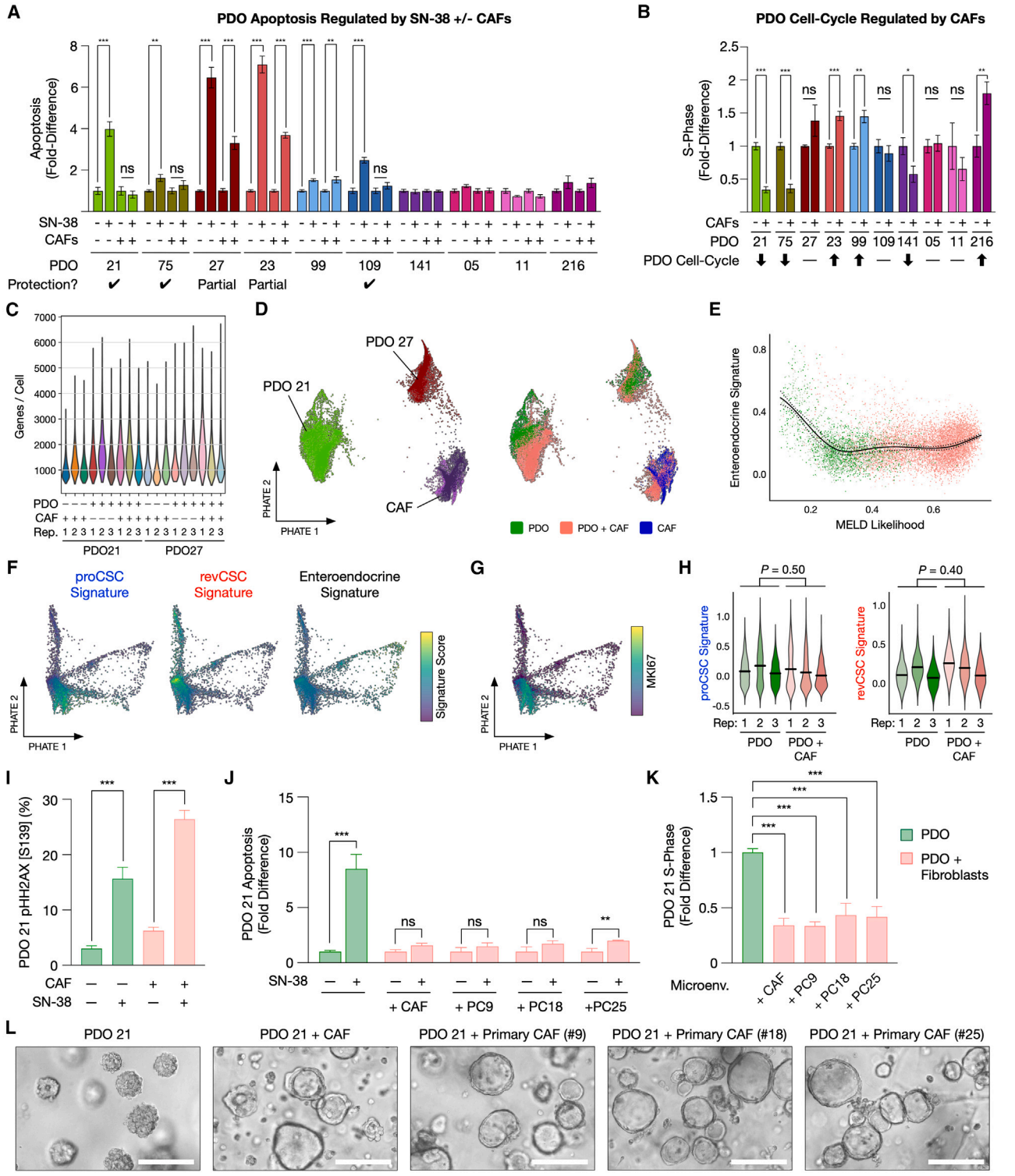

Figure S6. CAF-induced PDO cell-state shifts, related to Figures 5 and 6

(A) PDO SN-38-induced apoptosis +/− CAFs. Partial CAF protection is defined as a reduction in drug-induced apoptosis in co-culture relative to monoculture, yet apoptosis is still >1.5-fold over control and statistically significant.

(B) Fold difference to monoculture of PDO cells in S-phase when co-cultured with CAFs.

(C) Gene counts per cell for x18 scRNA-seq datasets.

(D) Single-cell PHATE of PDO 21 and PDO 27 +/− CAFs scRNA-seq.

(legend continued on next page)

(E) Enteroendocrine gene signature over MELD score.
(F) Single-cell PHATE of PDO 21 colored by proCSC, revCSC, and enteroendocrine gene signatures.
(G) Single-cell PHATE of PDO 21 colored by *MKI67*.
(H) procCSC and revCSC signatures in PDO 27 (low CAF protection) +/− CAFs. Unpaired *t* test.
(I) SN-38 induces on-target DNA double-strand breaks (DSBs) ($pHH2AX^+$) in PDO 21 irrespective of CAFs.
(J) PDO 21 chemoprotection via different primary CAFs derived from CRC patients.
(K) Fold difference to monoculture controls of PDO cells in S-phase when co-cultured with primary CRC CAFs. Unpaired *t* test, *** < 0.0001, ** < 0.001, * < 0.01. ns, not significant.
(L) PDO 21 morphology changes when co-cultured with different primary CRC CAFs.

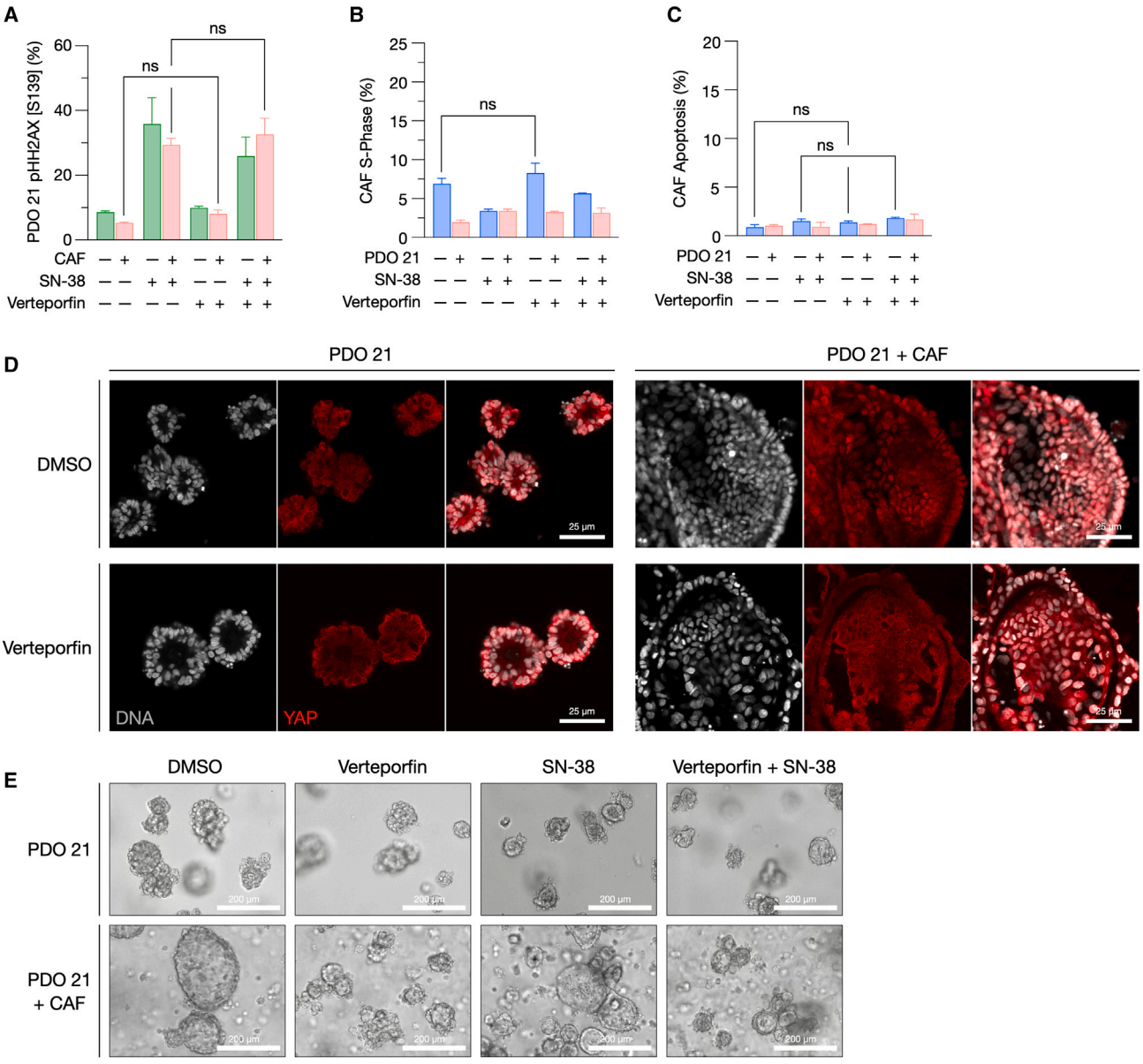

Figure S7. YAP inhibition of CAF-induced chemoprotection, related to Figure 6

(A) Verteporfin does not alter SN-38-induced on-target DNA-double strand breaks (pHH2AX^{+}) in PDOs.

(B and C) Verteporfin does not alter (B) S-phase or (C) apoptosis in CAFs. Unpaired *t* test; ns, not significant.

(D) CAF-induced nuclear translocation of YAP (red) to PDO nucleus (white) is reversed by Verteporfin. Scale bar, 25 μm.

(E) PDO 21 morphology +/− CAFs, +/− Verteporfin, +/− SN-38. Verteporfin reverses CAF-induced cyst-like morphology. Scale bar, 200 μm.